Stony Brook University

Neutral Atom Lithography with Metastable Helium

A Dissertation Presented

by

Claire Shean Allred

to

The Graduate School

in Partial Fulfillment of the Requirements

for the Degree of

Doctor of Philosophy

in

Physics

Stony Brook University

May 2009

Stony Brook University

The Graduate School

Claire Shean Allred

We, the dissertation committee for the above candidate for the Doctor of Philosophy degree, hereby recommend acceptance of this dissertation.

Harold Metcalf – Dissertation Advisor
Professor, Department of Physics and Astronomy

Gorge Sterman – Chairperson of Defense
Professor, Department of Physics and Astronomy

Clark McGrew
Professor, Department of Physics and Astronomy

Jon Longtin
Professor, Department of Mechanical Engineering
SUNY Stony Brook

This dissertation is accepted by the Graduate School.

Lawrence Martin
Dean of the Graduate School

Abstract of the Dissertation

Neutral Atom Lithography with Metastable Helium

by

Claire Shean Allred

Doctor of Philosophy

in

Physics

Stony Brook University

2009

In this dissertation we describe our performance of resist assisted neutral atom lithography using a bright beam of metastable 2^3S_1 Helium (He*). Metastable Helium atoms have 20 eV of internal energy making them easy to detect and able to destroy a resist. The He* is produced by a reverse flow DC discharge source and then collimated with the bichromatic force, followed by three optical molasses velocity compression stages. The atoms in the resulting beam have a mean longitudinal velocity of 1125 m/s and a divergence of 1.1 mrad. The typical beam flux is 2×10^9 atoms/mm^{2}s through a 0.1 mm diameter aperture 70 cm away from the source.

The internal energy of the atoms damages the molecules of a self assembled monolayer (SAM) of nonanethiol. The undisturbed SAM protects a 200 Å layer of gold that has been evaporated onto a prepared Silicon wafer from a wet chemical etch. Two methods are used to pattern the He* atoms before they destroy the SAM. First, a Nickel micro mesh was used to protect the SAM. These experiments established an appropriate dosage and etch time for patterning. The samples were analyzed with an atomic force microscope and found to have an edge resolution of 63 nm. Then, patterning was accomplished using the dipole force the atoms experience while traversing a standing wave of $\lambda = 1083\,\mathrm{nm}$ light tuned 500 MHz below the $2^3S_1 \rightarrow 2^3P_2$ transition. Depending on the intensity of the light, the He* atoms are focused or channeled into lines separated by $\lambda/2$. The lines cover the entire exposed length of the substrate, about 3 mm. They are about 3 mm long, corresponding to about twice the beam waist of the laser standing wave. Thus there are 6×10^3 lines of length 5500λ. These results agree with our numerical simulations of the experiment.

In loving memory of E. Townsend Shean Jr.

Contents

List of Figures

List of Tables

Acknowledgements

No work of any kind is completed in a vacuum, no matter how hard we try to suck the offending species of air from the steel cans that hold our atoms. For this reason, I will take a brief moment before the description of this work to reflect on how it was accomplished. As I recognize all the work that I did not perform in the completion of this dissertation I will inevitably omit some names and their contributions. Thus, these highlights are neither complete nor exclusive and for that I apologize.

First, I would like to thank my family. Without the emotional and financial support given by my parents through out my education this would not have been possible. The unwavering confidence that they, my sister Jessup and my extended family displayed in my ability to successfully complete this work even as our family faced its own share of challenges pushed me forward when I didn't know I was capable of continuing.

This work would have been impossible without my advisor, Hal Metcalf. He is an enthusiastic and effective teacher providing his students an environment conducive to their own maturation as physicists. I am more than fortunate to have had the opportunity to work with him.

The Department of Physics and Astronomy has an impressive army of fantastic people that work tirelessly to keep everyone's work running smoothly.

In the department office, Sarah Lutterbie, in addition to her official duties, serves as an advocate and cheerleader for the women who are attempting this course. Without Pat Peiliker mothering all of the graduate student through and correcting our stupid registration mistakes, I would have been in a great deal of administrative trouble. Linda Dixon and Pernille Jensen did paperwork magic behind the scenes. The departmental support network expands outside of the offices to Bob Segnini and Rich Bersak who, with a great deal of patience, facilitated the constant repair of our thermostats. Down the hall from our lab, Pete Davis kept the LN2 flowing and has at one point or another advised on the design or repair of my entire vacuum system and the detectors. Of course, none of the system would have been built without the guys in the machine shop. Mark Jablonski took the time to teach me the basics of design and how to stay safe around equipment; and Walter Schmeling and Jeff Slechta who are now joined by Jeffrey Thomas and Paul DiMatteo built everything. Last, but not least, Gene Shafto and Chuck Pancake in the electronics shop have more than managed my inability with all things electrical and my innate knack for breaking oscilloscopes.

For better or for worse Hal allows his students to rule the laboratory space. My most frightening experimental moment came a few months after joining the lab. Matt Partlow asked me to build an atomic detector. I showed him a design sketch which he glanced at and approved. I was struck that my dimensional measurements needed to be correct but there was no one that was going to second guess my numbers. Matt taught me the basics of what developed into my laboratory technique. As I have continued to fight with my wrenches, screwdrives, duct tape, cardboard and epoxy; Mike Keller helped

with the initial push and Jason Reeves has been there every step of the way. Marty Cohen has also been an invaluable source of knowledge and experience. Together with those that have gone before: Xiyue Miao, SeungHyun Lee, Andy Evil Guy Vernaleken, Esther Wertz and Ben Schaufenberger; and those who now take up the torch: Xiaoxu Lu, Chris Corder, Yuan Sun, Dan Stack and Jonathan who fought so hard; we have cussed, cried and laughed at our catastrophic failures and minute steps forward. I leave our experiment in good hands with Jason and Chris.

While us scientists tend to keep to our lab space, I am thankful for the friends who have pulled me away from my work and reminded me that I am still human. In Stony Brook, Sarah Campbell and Bjorg Larson have always been supportive of mischief and procrastination while Regina Caputo kept me sane with weekly "tennis" sessions. Kiersten Page and Kristina Anderson Wilmer have been my cheering squad from the south. Their phone calls and notes of encouragement helped me to laugh off and see the bright side of some of our larger lab disasters.

Finally, my husband, Chris. His unconditional dedication and patience over the last six and a half years leave me at a loss for words.

Chapter 1

Introduction

The demonstration of the laser in 1960 and its subsequent development opened vast areas of research; not the least of which is the study of atomic interactions with electromagnetic radiation. The study of atom-light interactions led to the laser cooling experiments of the 1980's. The fine control over atomic motion has resulted in elegant experiments demonstrating atomic clocks, the wave nature of atoms with Bose-Einstein Condensates and interference experiments, and the interchange of the traditional roles of light and matter with atom optical elements.

Atom based lithography offers a breadth of advantages and applications. The foremost of these is the use of light field based pattern generation and parallel fabrication. This results in patterns with minimal long range defects. Unlike electrons, neutral atoms are not suceptible to stray electric fields and the transverse deBroglie wavelength of cold atoms is several orders of magnitude smaller than that of the electron. This pushes the theoretical resolution limits of fabrication by the same factor. While atomic lithography may never

replace the more conventional methods for large-scale commercial fabrication, it may eventually provide a low dosage detector for atom optics and in turn more detailed insight into the interaction of various light fields with atoms.

1.1 Neutral Atom Lithography

The macroscopic patterning of neutral atoms with light and subsequent deposition onto a substrate was first demonstrated with Sodium in 1992 at Bell Labs [1] In addition to this direct deposition technique, patterning can also be accomplished with neutral atoms that chemically modify a surface. This resist-assisted neutral atom lithography requires a second etch step to transfer the image of the chemical change permanently into a surface. This technique has been widely demonstrated using light metastable noble gases [2–4], alkali metals [5], alkaline metals [6] and group III elements [7] patterend by a mesh to damage a self assembled monolayer (SAM) of alkanethiols on gold-coated silicon wafers.

When the neutral atoms damage un-protected areas of the SAM, the wetting properties in those areas are changed causing the underlying gold layer to be susceptible to a wet chemical etch [8]. The resolution of the resulting patterns from this technique, measured as the width of the edges in the patterns, is approximately 100 nm and seems to be limited by the properties of the gold layer and the action of the etch. The resist-assisted atom lithography technique has also been applied to different types of positive and negative resists on different substrates [4, 9–12].

Both the direct deposition and resist assisted lithography techniques have

also been used to create structures whose periodicity is determined optically. In these experiments a one or two dimensional optical standing wave (light mask) channels the atoms into its nodes before depositing them onto the substrate [13–16]. Alternatively, the light mask can be used to change the internal state of the atom so that it no longer affects the resist [17, 18]. The periodicity of such patterns are known to the accuracy of the frequency of the light, which is typically locked to an atomic transition [19, 20]. The light mask technique has also been expanded to take advantage of the rich internal structure of neutral atoms. Patterns that are independent of the light mask wavelength [21] and patterns with periodicity less than half the light mask wavelength [22, 23] have also been demonstrated.

1.2 The Two Level Atom

The two level problem is covered in many quantum mechanics texts [24, 25]. Here we will briefly justify its application to an atomic system and explore the methods of looking at the problem.

The simplest atom is Hydrogen consisting of a proton and an electron. The interaction between the two constituent particles and subsequent structure of the atom is to a first approximation governed by the Coulomb interaction. This results in the Hamiltonian

$$\mathcal{H}_o = -\left(\frac{\hbar^2}{2m_e} \bigtriangledown^2 + \frac{e^2}{4\pi\epsilon_o}\frac{1}{r}\right) \tag{1.1}$$

which describes the attraction of the electron to the proton in the absence of

any external fields. Taking the mass of the proton to be infinite, the solution of the time independent eigenvalue problem in a spherical coordinate system gives the energy levels

$$E_n = -\left[\frac{m_e}{2\hbar^2}\left(\frac{e^2}{4\pi\epsilon_o}\right)^2\right]\frac{1}{n^2} = -\frac{mc^2\alpha^2}{2n^2} \tag{1.2}$$

where $\alpha = \frac{e^2}{4\pi\epsilon_o\hbar c}$. Solving the fully time dependent Schrödinger equation gives the wave functions:

$$\Psi_n(\boldsymbol{r},t) = \sqrt{\left(\frac{2}{na}\right)^3\frac{n-l-1}{2n[(n+1)!]^3}}e^{\frac{-r}{na}}\left(\frac{2r}{na}\right)^2 L^{2l+1}_{n-l-1}\left(\frac{2r}{na}\right)Y_{lm}(\theta,\phi)e^{-\imath E_n t/\hbar}, \tag{1.3}$$

where $Y_{lm}(\theta,\phi)$ are the spherical harmonics and L^{2l+1}_{n-l-1} are the associated Laguerre polynomials. Adding further corrections to the Hamiltonian accounting for the relativistic nature of the motion of the electron and the interaction of moving charges with the magnetic fields they create, lifts the degeneracy of the angular parts of the wave function. The result is the Hydrogen spectrum with a rich structure of differently spaced energy levels.

The unperturbed energy levels from Eq. 1.2 are the physical states in which the atom is found when measured in the laboratory. Using the bra-ket notation the time independent eigenvalue problem can be restated

$$\mathcal{H}_o|n\rangle = E_n|n\rangle. \tag{1.4}$$

where $|n\rangle$ is time independent and a member of the complete set of atomic wave functions. Any external field applied to the atom will change the wave

functions and the energies. This problem is then written as

$$[\mathcal{H}_o + \mathcal{H}']|\psi(\boldsymbol{r},t)\rangle = E|\psi(\boldsymbol{r},t)\rangle \tag{1.5}$$

where the new eigenfunctions can be represented in the basis formed by the unperturbed eigenfunctions

$$|\psi(\boldsymbol{r},t)\rangle = \sum_n c_n e^{-\imath E_n t/\hbar}|n\rangle \tag{1.6}$$

and we have separated the space and time parts of the unperturbed states. If the perturbation is time dependent, the new eigenfunctions will be time dependent mixtures of the unperturbed eigenfunctions, resulting in laboratory observed transitions between the known stationary states.

Under a time dependent perturbation the probability of observing specific stationary states is given by $|c_n(t)|^2$, with the time dependence of $c_n(t)$ derived from the time dependence of $\mathcal{H}'$. In order to calculate these populations the eigenvalue equation is applied to both sides of Eq. 1.6

$$[\imath\hbar\frac{\partial}{\partial t} - \mathcal{H}_o - \mathcal{H}']|\psi(t)\rangle = [\imath\hbar\frac{\partial}{\partial t} - \mathcal{H}_o - \mathcal{H}']\sum_n c_n(t)e^{-\imath E_n t/\hbar}|n\rangle. \tag{1.7}$$

The projection of the perturbed eigenvector onto the original stationary states is calculated to solve for $c_n(t)$.

$$\imath\hbar\dot{c}_m(t) = \sum_n \langle m|\mathcal{H}'|n\rangle e^{\imath\omega_{mn}t}c_n(t) \tag{1.8}$$

where $e^{-\imath E_m t/\hbar}|m\rangle$ is another stationary state and $\omega_{mn} \equiv \frac{E_m - E_n}{\hbar}$. In the event

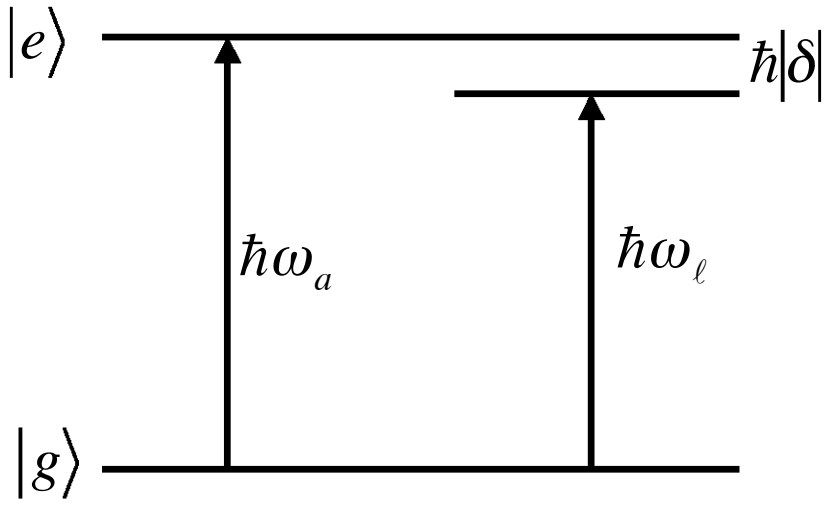

Figure 1.1: Simplified energy levels of the two level atom. The ground $|g\rangle$ and excited $|e\rangle$ states are separated by $\hbar\omega_a$. Laser light couples the two states, and can be detuned from the resonance by $\delta \equiv \omega_l - \omega_a$.

that the spectrum of the perturbation is narrow and centered close to the energy splitting of two specific states, we can make the approximation that the rest of the states give a negligible contribution to the perturbed eigen vector. Thus we are left with a two level atomic system.

1.2.1 Rabi Oscillations

For the purpose of this discussion, the time dependent perturbation is taken to be the oscillating electric field from a light source. The states are now renamed $|g\rangle$ and $|e\rangle$ for ground and excited; and the laser detuning is defined as $\delta = \omega_{laser(l)} - \omega_{atom(a)}$ (See Fig. 1.1). If we make the approximation that the perturbing electric field does not vary appreciable over atomic length scales

and $\delta \ll \omega_a, \omega_l$, we can calculate the atomic distribution

$$c_g(t) = (\cos\frac{\Omega' t}{2} - \imath\frac{\delta}{\Omega'}\sin\frac{\Omega' t}{2})e^{\imath\delta t/2} \tag{1.9a}$$

$$c_e(t) = -\imath\frac{\Omega}{\Omega'}\sin\frac{\Omega' t}{2}e^{-\imath\delta t/2} \tag{1.9b}$$

where we have defined the Rabi frequency as

$$\begin{aligned} \Omega &\equiv -\frac{1}{\hbar}\langle e|e\overrightarrow{\mathcal{E}}(\boldsymbol{r},t)\cdot\overrightarrow{r}|g\rangle \\ \Omega' &\equiv \sqrt{\Omega^2+\delta^2}. \end{aligned} \tag{1.10}$$

As light resonant with the $g \rightarrow e$ transition is incident on the atom, it coherently oscillates between the ground and excited states at the Rabi frequency Ω. As the light is tuned off resonance, the oscillations become faster and the excited state is never fully populated ($c_e(t) < 1$, See Fig. 1.2).

1.2.2 The Light Shift

Adding an off diagonal perturbation to the Hamiltonian of any pure state system not only changes the wave functions, it also shifts the original energy levels. For the case of light on atoms this is called the light shift, as the perturbation is typically the light field. The time dependence adds complications to the calculation which can be avoided by transforming the resulting differential equations from Eq. 1.8 into a frame rotating at the frequency of the light.

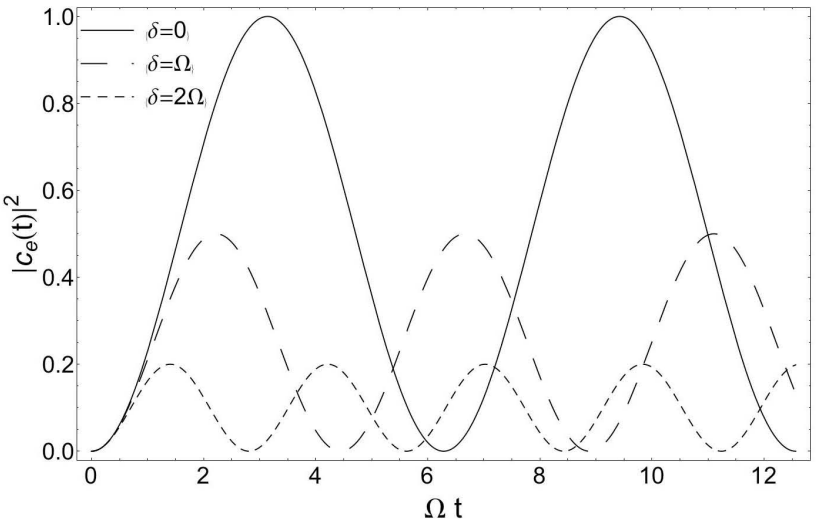

Figure 1.2: Probability that the atom will be in the excited state.

With this transformation amplitudes of the pure states become

$$\begin{aligned} c'_g(t) &\equiv c_g(t) \\ c'_e(t) &\equiv c_e(t)e^{\imath\delta t}. \end{aligned} \tag{1.11}$$

which absorbs the time dependence of the perturbing light into the amplitudes of the states. Thus the perturbation becomes effectively time independent. With this substitution, Eq. 1.8 becomes

$$\imath\hbar\frac{\mathrm{d}c'_g(t)}{\mathrm{d}t} = c'_e(t)\frac{\hbar\Omega}{2} \tag{1.12a}$$

$$\imath\hbar\frac{\mathrm{d}c'_e(t)}{\mathrm{d}t} = c'_g(t)\frac{\hbar\Omega}{2} - c'_e(t)\hbar\delta. \tag{1.12b}$$

and the Hamiltonian, now time independent, becomes

$$\mathcal{H} = \frac{\hbar}{2}\begin{pmatrix} -2\delta & \Omega \\ \Omega & 0 \end{pmatrix} \tag{1.13}$$

which when diagonalized gives the energy shifts for the ground and excited states: $E_{g,e} = \hbar(-\delta \mp \Omega')/2$, where Ω' is defined in 1.10.

1.2.3 The Bloch Sphere

Another powerful tool for describing the state of a two level atom is the Bloch vector. The components of the Bloch vector are the expectation values of the Pauli spin matricies in a two level system

$$\overrightarrow{R} = (c_g c_e^* + c_g^* c_e,\ \imath(c_g c_e^* - c_g^* c_e),\ |c_e|^2 - |c_g|^2). \tag{1.14}$$

In the frame rotating at ω_l, the first two components $\langle\sigma_x\rangle$ and $\langle\sigma_y\rangle$ are the in phase and in quadrature response of the atomic dipole moment. The third component is the probability difference of the atomic state population. While it is not an obvious calculation, in order to conserve probability the length of the Bloch vector is 1 and it evolves on a unit sphere (See Fig. 1.3).

The time dependence of the c_g's and c_e's indicate that while it does not change in length, the Bloch vector does have a time dependence. Using eqns. 1.8 it is apparent that the Bloch vector can be described as evolving under the influence of a torque

$$\frac{\mathrm{d}\overrightarrow{R}}{\mathrm{d}t} = \overrightarrow{\Omega} \times \overrightarrow{R} \tag{1.15}$$

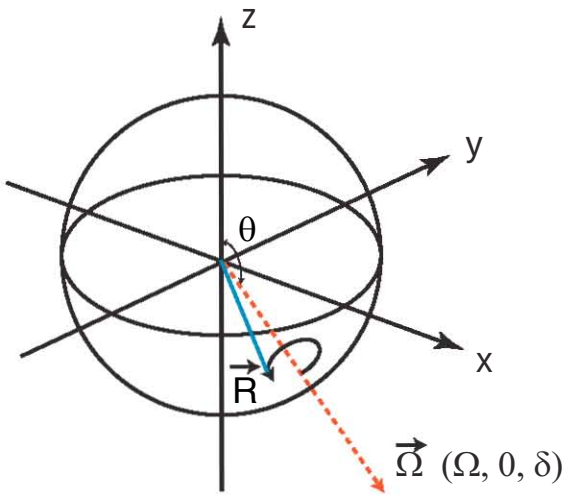

Figure 1.3: The optical Bloch equations determine the motion of the Boch vector which is confined to the surface of a unit sphere.

when that torque vector is defined as

$$\overrightarrow{\Omega} = (\mathrm{Re}(\Omega),\ \mathrm{Im}(\Omega),\ \delta). \tag{1.16}$$

This formalism combined with the density matrix notation eventually produces the Optical Bloch Equations (OBE's) without spontaneous emission. Because spontaneous emission is not a coherent process accounted for in the perturbing Hamiltonian, it must be added to the OBE's using various argu-

ments and results in equations of the following form:

$$\begin{aligned}
\frac{\mathrm{d}\rho_{gg}}{\mathrm{d}t} &= \gamma\rho_{ee} + \frac{\imath}{2}(\Omega^*\tilde{\rho}_{eg} - \Omega\tilde{\rho}_{ge}) \\
\frac{\mathrm{d}\rho_{ee}}{\mathrm{d}t} &= -\gamma\rho_{ee} + \frac{\imath}{2}(\Omega\tilde{\rho}_{ge} - \Omega^*\tilde{\rho}_{eg}) \\
\frac{\mathrm{d}\tilde{\rho}_{ge}}{\mathrm{d}t} &= -(\frac{\gamma}{2} + \imath\delta)\tilde{\rho}_{ge} + \frac{\imath}{2}\Omega^*(\rho_{ee} - \rho_{gg}) \\
\frac{\mathrm{d}\tilde{\rho}_{ge}}{\mathrm{d}t} &= -(\frac{\gamma}{2} - \imath\delta)\tilde{\rho}_{ge} + \frac{\imath}{2}\Omega(\rho_{gg} - \rho_{ee})
\end{aligned} \tag{1.17}$$

where $\rho_{gg} = c_g c_g^*$, $\rho_{ee} = c_e c_e^*$, $\tilde{\rho}_{ge} = c_g c_e^* e^{-\imath\delta t}$, and $\tilde{\rho}_{eg} = c_e c_g^* e^{-\imath\delta t}$, and γ is defined in Eq. 1.18. These equations govern the evolution of the atomic state in the presence of spontaneous emission.

1.3 Monochromatic Forces

1.3.1 The Radiative Force

When an atom encounters light that is resonant with the ground to excited state transition, there is a probability that the atom will absorb the light. As shown in Eq. 1.9 the probability is dependent on the coupling strength of the light to the transition. With that absorption the atom now has the energy $\hbar\omega$ and momentum $\hbar k$ of the light. While the energy is stored in the internal state of the atom, the momentum kick results in a small velocity change for the atom in the direction the absorbed light was originally traveling. After a certain amount of time,

$$\tau \equiv \frac{1}{\gamma} = \frac{\omega_a^3 \mu^2}{3\pi\epsilon_o \hbar c^3}, \tag{1.18}$$

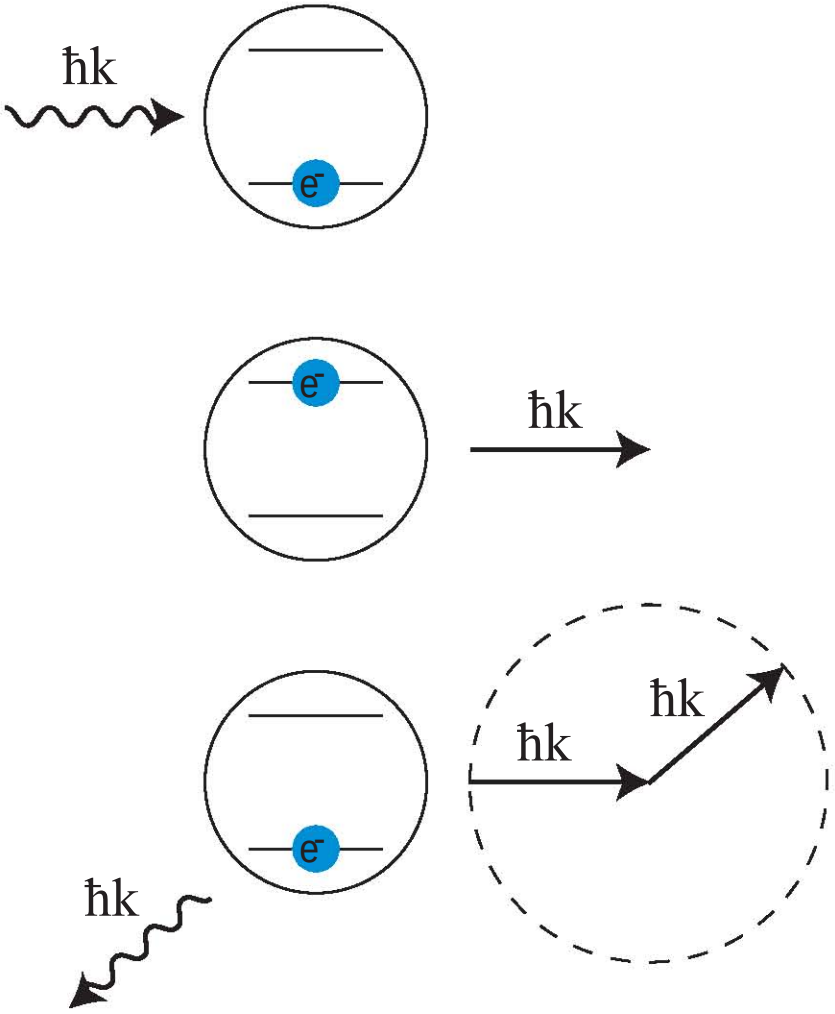

Figure 1.4: The steps of the cycle that produces the scattering or radiative force. The top picture is just a two level atom in a monochromatic laser light field. The atom is excited by absorption and receives a momentum kick $\hbar\overrightarrow{k}$. Spontaneous emission is spatially symmetric and after many repeated cycles the associated momentum kick averages to zero.

where $\mu = e\langle e|\overrightarrow{r}|g\rangle$ is the dipole moment between the two levels, the atom will spontaneously emit the absorbed light in a random direction. The internal energy will leave with the light and the resulting momentum kick will be in the opposite direction of the emitted light (See Fig. 1.4). The atom is left in the ground state and ready to absorb more light. Each time the atom absorbs light it receives a kick in the direction of light propagation. The random direction of the spontaneous emission kicks average to zero. Thus momentum steps from absorption, $\hbar k$, over the interaction time, $1/(\gamma\rho_{ee}) \equiv 1/\gamma_p$, give the radiative force

$$F = \hbar k\gamma_p = \hbar k \frac{s_o\gamma/2}{1 + s_o + (2(\delta - |\omega_D|)/\gamma)^2} \tag{1.19}$$

where $s_o \equiv 2|\Omega|^2/\gamma^2$ is the on resonance saturation parameter for the transition and $\omega_D \equiv -\overrightarrow{k} \cdot \overrightarrow{v}$ is the Doppler frequency shift due to the movement of the atoms. As the intensity of the light is turned up the force gets larger until the scattering rate γ_p saturates to $\gamma/2$. The force has a maximum value of $F_{rad,max} = \hbar k\gamma/2$.

1.3.2 Optical Molasses

In the limit of low intensity and small detuning the radiative force from light propagating in multiple directions can be added. For the case of counter propagating light, the forces are in opposite directions. Taking into account the detuning of atomic resonance due to the motion of the atoms, the resulting addition gives

$$\overrightarrow{F} = \hbar\overrightarrow{k}\frac{s_o\gamma/2}{1 + s_o + (2(\delta - |\omega_D|)/\gamma^2} - \hbar\overrightarrow{k}\frac{s_o\gamma/2}{1 + s_o + (2(\delta + |\omega_D|)/\gamma^2}. \tag{1.20}$$

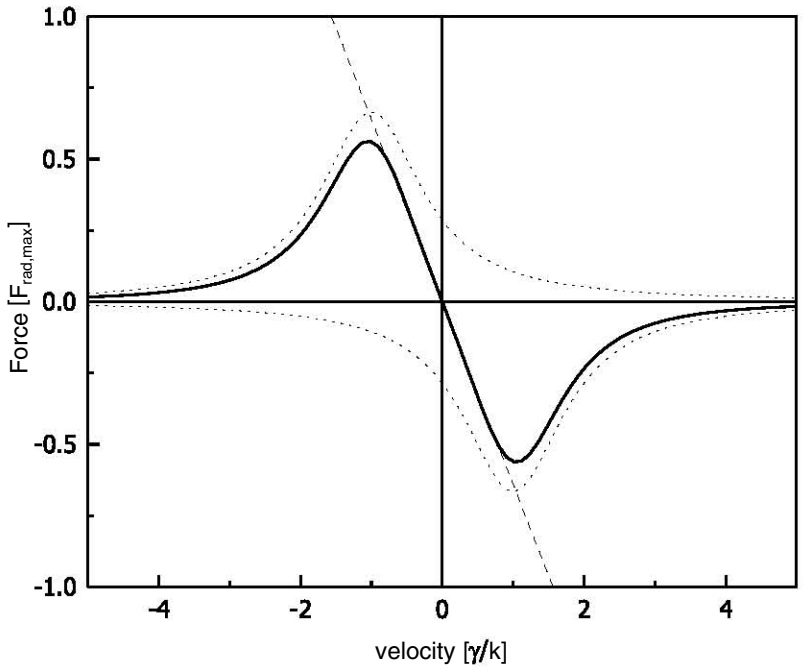

Figure 1.5: The velocity dependence of the force in optical molasses that results from two counter-propagating red-detuned laser beams.

This gives a force profile that is dependent on the velocity of the atoms (Fig. 1.5). Within the velocity limits $|v| < \gamma/k$ the force behaves approximately linearly. With the approximation that terms of the order $(kv/\gamma)^4$ are negligible, the force takes the form

$$\overrightarrow{F}_{OM} \equiv \frac{8\hbar k^2 \delta s_o \overrightarrow{v}}{\gamma(1 + s_o + (2\delta/\gamma)^2)^2} \equiv -\beta \overrightarrow{v}. \tag{1.21}$$

When $\delta < 0$ the damping force opposes the motion of the atoms and can be used to cool them.

A first look at the force profile in Fig. 1.5 suggest that optical molasses can achieve an ultimate temperature of 0 K. This does not occur because while the average directionality of the spontaneous emission steps is zero, the root mean square value is not. In order to take this into account for an ultimate temperature calculation we can use a "hand-waving" argument and equate the rate of cooling from absorption and rate of heating from emission [26]. When the cooling and heating steps reach a steady state, the resulting final temperature is

$$T_D = \frac{\hbar\gamma}{2k_B}. \tag{1.22}$$

When the values of δ and s_o get large, the simple picture of one absorption followed by spontaneous emission is no longer valid. In the high intensity limit stimulated emission of the atom into one of the light fields needs to be taken into account. In this regime the force can be calculated by using the density matrix formalism [27] to describe the atomic state. The result is a convergent continued fraction and is still velocity dependent. The velocity action range is broadened with the directionality of the force dependent on velocity, intensity

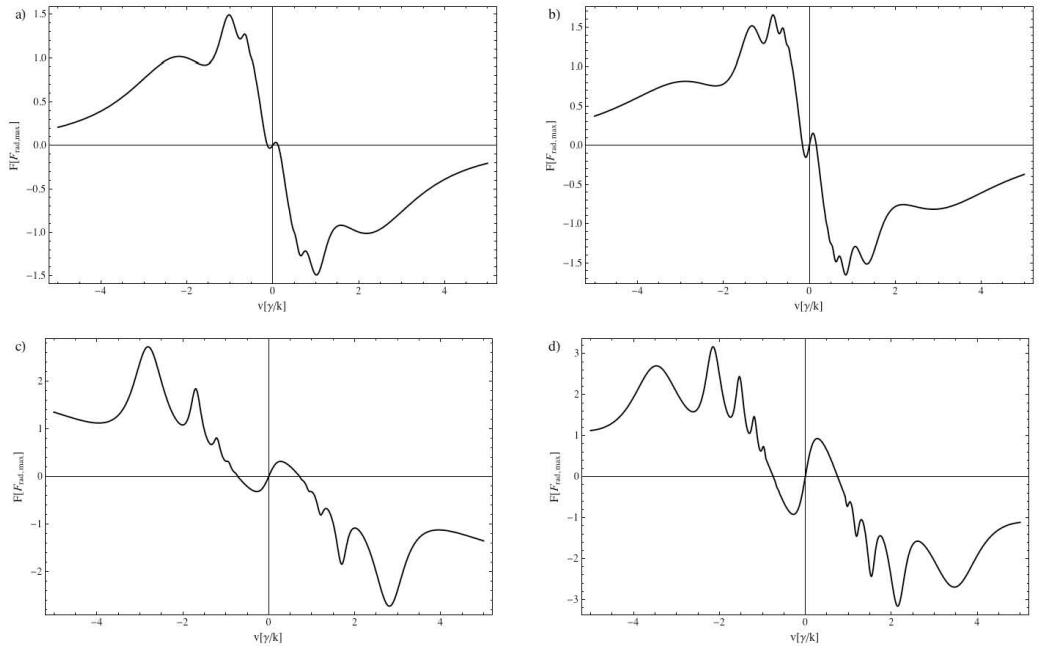

Figure 1.6: Non-linear and multi-photon processes occur at high intensities broadening the capture range and switching the direction of the force. Force profiles are calculated with the continued fraction method presented in [27]. (a) $\delta = -1.2\gamma, \mathrm{s}_o = 10$ (b) $\delta = -1.2\gamma, \mathrm{s}_o = 20$ (c) $\delta = -5\gamma, \mathrm{s}_o = 50$ (d) $\delta = -5\gamma, \mathrm{s}_o = 100$.

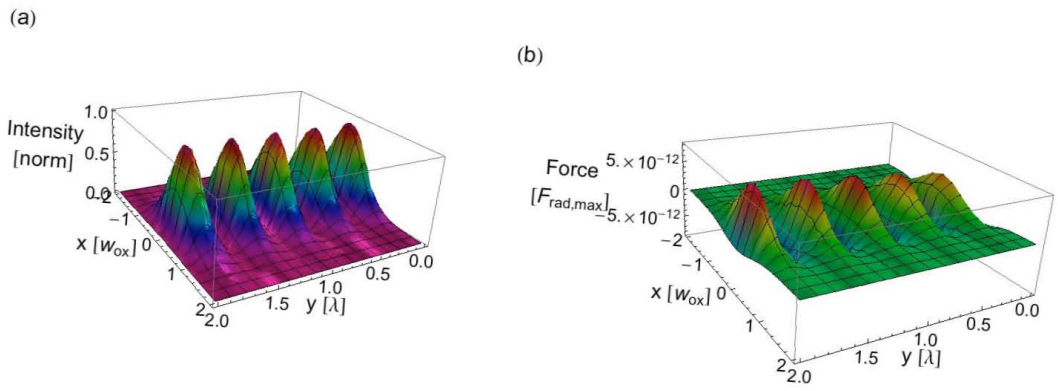

Figure 1.7: (a) Normalized intensity of a standing wave light field at z=0 created by light traveling in the y direction with a mirror at y=0.
(b) Force on atoms in the center of the light field when $\delta > 0$. The atoms are forced to the nodes of the standing wave. The force changes direction over the range of a wavelength, thus the spatial average of the dipole force goes to zero.

and detuning (Fig. 1.6).

1.3.3 The Dipole Force

In a traveling wave light field there is no spatial variation of intensity, but in a standing wave light field the intensity is spatially modulated depending on the phase and polarization of the counter-propagating light. This results in a spatial modulation of the separation of the energy levels arising from the light shift, described in Sec. 1.2.2. In the event that the detuning is large compared to the Rabi frequency ($|\delta| \gg |\Omega|$), the light shift is given by [28]

$$\Delta E_g = \frac{\hbar\Omega^2}{4\delta} . \tag{1.23}$$

The dipole force arises from the gradient of the energy levels. When the Rabi

frequency for each beam is related to the intensity,

$$\Omega = \gamma\sqrt{\frac{I}{2I_{sat}}}, \tag{1.24}$$

and a generic form of $I(z) = I_o \cos^2(kz)$ is taken for the intensity of the standing wave of light; the dipole force is given by:

$$F_{dip} = -\frac{\partial}{\partial z}\Delta E_g = -\frac{\partial}{\partial z}\left(\frac{\hbar\gamma^2}{8\delta}\frac{I}{I_{sat}}\right) = \frac{\hbar k\gamma^2 I_o}{8\delta I_{sat}}\sin(2kz). \tag{1.25}$$

Within the limits of this approximation the dipole force is similar to the radiative force in that its direction is dependent on the sign of δ. Yet, unlike the radiative force and optical molasses, the dipole force is not restricted by the decay rate of the atom and does not switch direction with increasing power. The action of the force is limited in that it is conservative and changes direction over the range of wavelength. Thus the spatial average of the force is zero, and it can not be used for cooling.

1.4 Polychromatic Forces

1.4.1 Adiabatic Rapid Passage

Adiabatic Rapid Passage (ARP) is a well known population inversion technique from magnetic resonance studies. ARP is induced with careful control of the torque vector in Eq. 1.15. The torque vector is induced to move slowly across the Bloch sphere such that the Bloch vector can follow it. The process must be completed rapidly enough that the system does not lose coherence by

spontaneous emission.

In an atomic system, the torque vector is controlled by the light field. Taking the Rabi frequency to be real, the torque vector from Eq. 1.16 is $\overrightarrow{\Omega} = (\Omega, 0, \delta)$. By simultaneously pulsing the light and sweeping its frequency from way below to way above the transition resonance, the torque vector moves from the bottom of the Bloch sphere to the top. Thus, the atomic system is taken completely from its initial state to a final state.

The use of ARP to control the motion of atoms has been studied extensively [29–31]. ARP is translated to an atomic force by giving directionality to the population inversions. As in the monochromatic picture from Section 1.3.2, the population inversion is associated with a momentum kick of $\hbar k$ given to the atom. If the inversion is from the ground to the excited state, the momentum kick is in the direction of the inverting pulse; and if the inversion is from the excited state back to the ground state the momentum kick is in the opposite direction of the inverting pulse. In the event the atom remains in the excited state between the action of two pulses come from opposite directions, the atom receives a momentum kick of $2\hbar k$. The repetition rate of this process is limited by the characteristics of the pulses and, by definition, has to occur more quickly than the spontaneous emission rate. Thus, the magnitude of the force is much greater. At the moment, there has not yet been made a measure of the velocity capture range of the force.

1.4.2 The Bichromatic Force

When light has equal amounts of two different co-propagating frequencies the resulting light can be viewed as an amplitude modulated traveling wave where the carrier frequency is

$$\frac{\omega_1 + \omega_2}{2} \tag{1.26}$$

and the envelope frequency is

$$\frac{\omega_1 - \omega_2}{2} \equiv \delta_{bichro}. \tag{1.27}$$

If the carrier frequency is set to atomic resonance, the power and δ_{bichro} can be changed so the amplitude modulation fulfills the π pulse condition. In order to do that, the power and δ_{bichro} are constrained such that

$$\Omega = \frac{\pi \delta_{bichro}}{4}. \tag{1.28}$$

In this field both excitation and de-excitation are coherent processes with a repetition time of π/δ_{bichro}, which is the period of the amplitude modulation.

When two modulated fields are counter propagating, the atom can absorb from one field receiving a momentum kick of $\hbar k$ and then coherently emit into the other field receiving another momentum kick of $\hbar k$ in the same direction as the first one (Fig. 1.8). The resulting force

$$F = \frac{\Delta p}{\Delta t} = \frac{2\hbar k \delta_{bichro}}{\pi} \tag{1.29}$$

is not limited by the properties of the atom so it can be tuned to be very large.

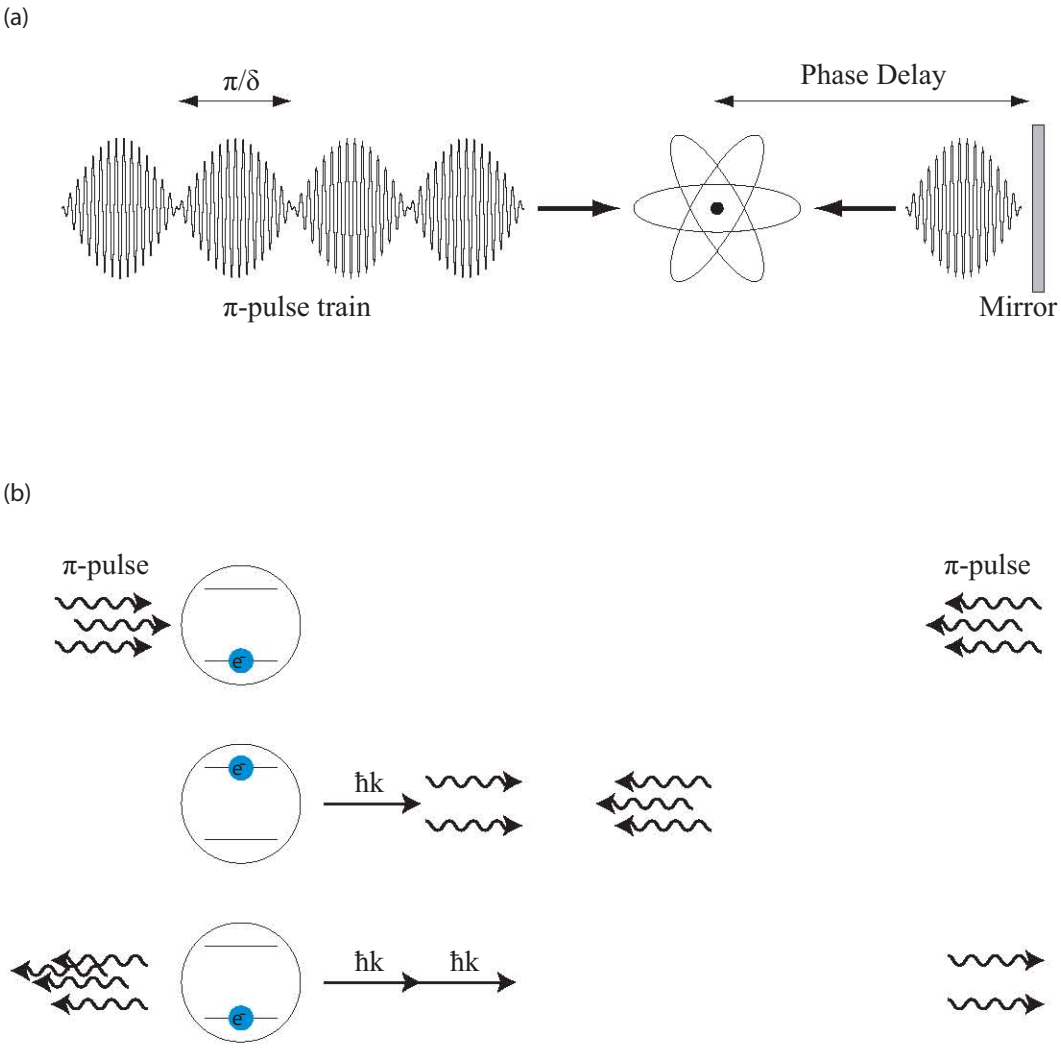

Figure 1.8: The atom absorbs from one beam receiving a momentum kick of $\hbar k$ and emits into the other receiving another $\hbar k$ in the same direction.

This initial picture does not take into account the atom's propensity to decay naturally from the excited to the ground state. In the event of spontaneous emission the direction of the force on the atom switches because instead of receiving two momentum kicks in the same direction, the atom receives a kick in the "wrong" direction from the pulse originally intended to cause stimulated emission. With spontaneous emission occurring, the resulting changes in the directionality of the force cause it to be averaged to zero. Directionality can be introduced to the system by offsetting the phase between the counter-propagating pulses so that in a chosen direction for the force the atom spends less time in the excited state so it is less likely to spontaneously decay when it is going the correct direction and more likely to spontaneously decay when it is going the incorrect direction. An initial guess puts the phase offset at $\pi/4$.

In practice the force profiles must be calculated by numerical integration of the optical Bloch equations (See Fig. 1.9). The resulting optimum Rabi frequency is

$$\Omega = \sqrt{\frac{3}{2}}\delta_{bichro}, \tag{1.30}$$

and the force is approximately 3/4 of the peak value predicted by the π pulse model. While attractive, the π pulse model cannot be viewed as a complete description of the atom light interaction. In the experiment, π pulses are not temporally separated and the light fields are strong so non-linear processes occur. Regardless, the π pulse model gives a very intuitive description of the force action and the numerical calculations show the force is maximized for phase offsets suggested from that model.

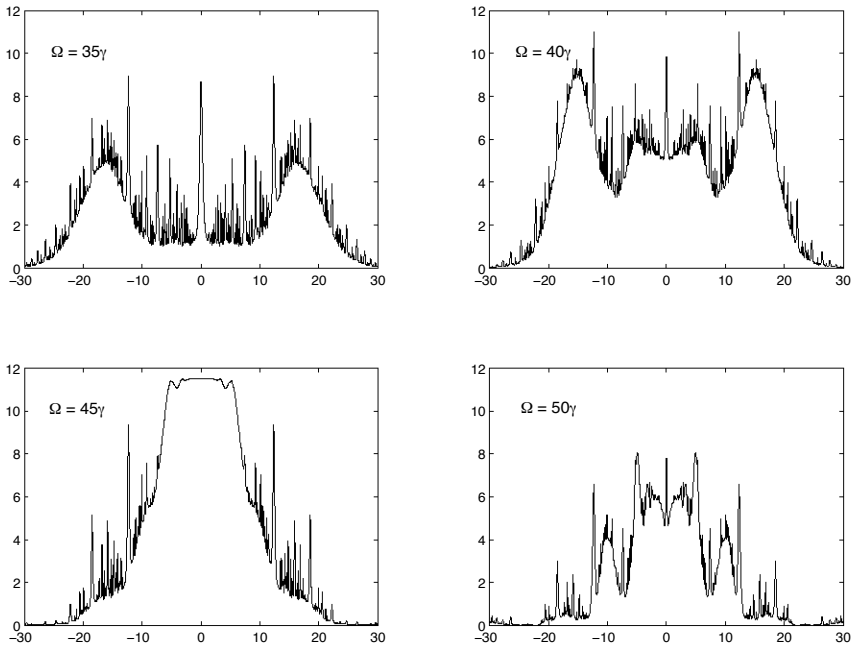

Figure 1.9: Force profiles from the bichromatic force are obtained by numerical integration of the OBE's.

1.5 Structure of Helium

The energy difference of 19.98 eV between the 1^1S state and the 2^3S state of Helium is equivalent to a wavelength of 63 nm. In addition to this transition being inaccessible for excitation with current optical techniques, it is a doubly-disallowed transition. The lack of angular momentum change and the spin change required violate the electric dipole transition selection rules. This results in the metastability of the 2^3S state (lifetime of $\sim 8000\,\mathrm{s}$) which for the purpose of this experiment is the ground state of He*. Collisions are its primary mode of decay to the ground state of He.

There are two easily optically accessible transitions from the ground state of He* as shown in the simplified level diagram of He in Fig. 1.10. All of the He* collimation and lithography experiments use the $2^3\mathrm{S}_1 \rightarrow 2^3\mathrm{P}_2$ transition near $\lambda = 1083$ nm, the light production for which is discussed in Ch. 2. He* control experiments also conducted in our laboratory have been performed on the $2^3\mathrm{S}_1 \rightarrow 3^3\mathrm{P}_2$ transition. These experiments and the procedure for production of $\lambda = 389$ nm light are discussed elsewhere [32–34]. Since the nuclear spin of ^{4}He is zero, there is no hyperfine structure and only the magnetic sublevels affect the transition.

With the proper polarization tailoring of the light field, both of those transitions cycle on one set of the magnetic sub-levels. Thus, in the control experiments, He* can be treated as a two level atom.

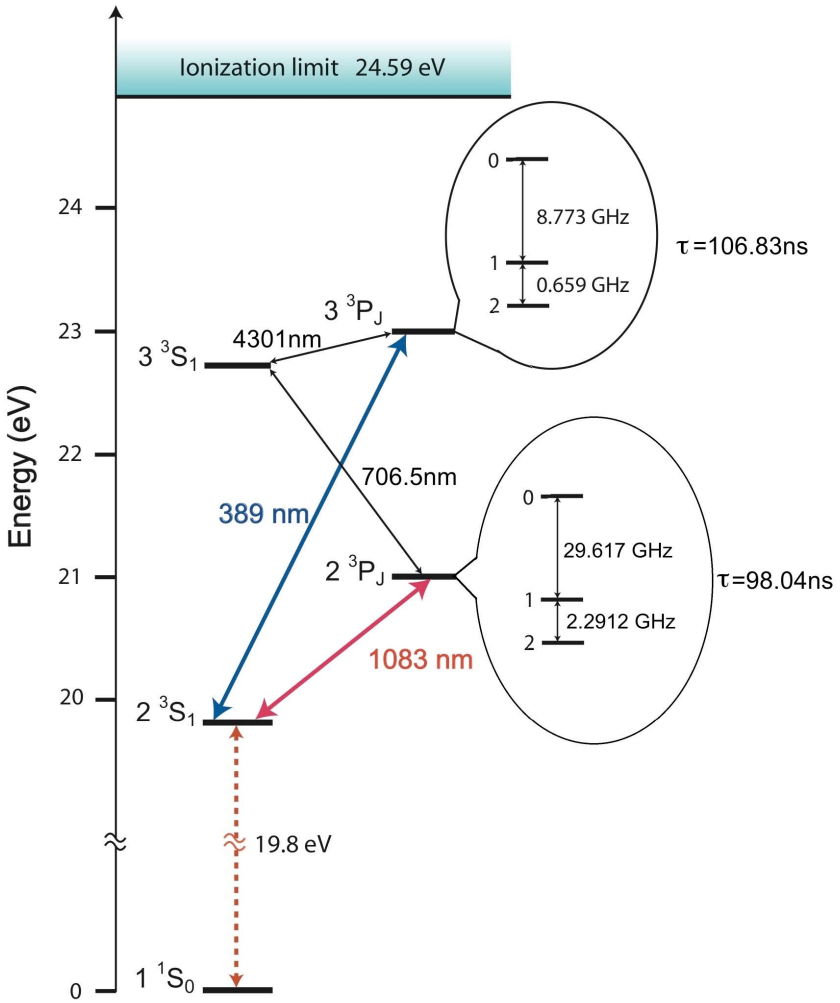

Figure 1.10: There are two optically accessible transitions in He*.

	λ (nm)	$\hbar\omega_a$ (eV)	τ (ns)	$\gamma/2\pi$ (MHz)	I_{sat} (mW/cm^2)	$\omega_r/2\pi$ (kHz)
$2^3S_1 \rightarrow 2^3P_2$	1083.33	1.144	98.04	1.62	0.17	42.46
$2^3S_1 \rightarrow 3^3P_2$	388.98	3.187	106.83	1.49	3.31	329.35

Table 1.1: Some properties of the two optically accessible transitions from the metastable state.

Chapter 2

Light System

All of the light control for the atomic collimation and subsequent patterning targets the $2^3S_1 \rightarrow 2^3P_2$ transition in Helium. The observed vacuum wavelength for this transition is 1083.331 nm with a spectral width of 1.6 MHz. This lies near standard communications wavelengths; thus, much of the equipment we use was primarily developed for the communications industry and then adapted to our experiment.

The differing spectral demands of atomic collimation and lithographic patterning require separate light sources which exhibit enough similarities that they can be described in parallel.

2.1 Diode

The collimation and patterning light both are supplied by Spectra Diode Labs (SDL) model SDL-6702-H1 distributed Bragg reflector (DBR) diodes. The SDL diodes are packaged in an 8 pin TO-3 window mount with a thermistor

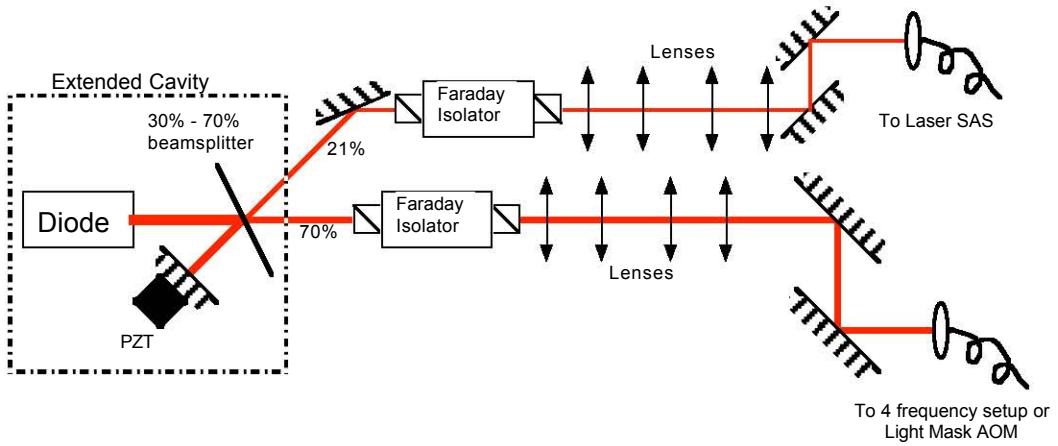

Figure 2.1: Schematic of the diode laser setup. 9% of the output is reflected back into the diode in order to narrow the linewidth. Faraday isolators prevent uncontrolled feedback from destabilizing the diode. The shaped light is launched into fibers for ease of transportation and mode cleaning.

and a thermoelectric cooler. These diodes supply approximately 20 mW of single mode 1083 nm light. The grating blazed on the back facet of the diode acts as a wavelength selective mirror narrowing the typical diode laser bandwidth of 2-4 nm to a few MHz. In order to bring the bandwidth of the laser to less than the width of the He* transition; 30% of the diode output is picked off by a plate beamsplitter and sent to a retro reflecting mirror mounted on a piezo-electric transducer (PZT): See Fig. 2.1. This controlled feedback mechanism extends the lifetime of selected photons in the cavity and thus narrows the bandwidth down to 125 kHz [29]. The result of this cavity setup is that each diode produces two beams: a main beam (70% full power) and a leakage beam (21% full power). Both beams out of both lasers exhibit the characteristic divergence of diode light and must collimated with both spherical and cylindrical telescopes. In order to protect the extended cavity from disruptive

external feedback, optical isolators are placed in all four beams: OFR IO-3-1083-HP for the main beams and OFR IO-D-1080-Z for the leakage beams. After the optical isolators and collimation optics, all four beams are launched into single mode optical fibers. This is done for ease of light transportation and so that further tailoring on the light is simplified by the use of the lowest Gaussian mode.

The frequency tuning and output power of the diode depend on its temperature, drive current and external cavity length. In order to shield the diodes from vibrations and external temperature fluctuations, they are mounted on a 305 mm x 710 mm x 76 mm Aluminum slab which is housed inside a box constructed with polystyrene foam insulation. This setup, along with further stabilization efforts, maintains a power stability to within 10 % of the output peak. While the above mentioned controls, in addition to the lab weather, are not fully un-coupled in their effect on the diode performance; they can be treated as coarse, medium and fine tuning for the diode frequency.

The temperature of the diode determines the size of its active region and can be viewed as the coarse frequency tuning. While both diodes saw first light in 1997 [29] they have experienced a different amount of use and as a result must be tuned separately. The diode that seeds the collimation is temperature stabilized to 24.1 ± 0.1°C with an ILX Lightwave LDT-5910 controller. The electronics for the diode that seeds the light mask are slightly different. The temperature of the light mask (LM) diode is set using a Newport model 325 temperature controller which holds the thermistor in the temperature control circuit to 9.73 kΩ.

The drive current of the diode not only determines the output power, but it

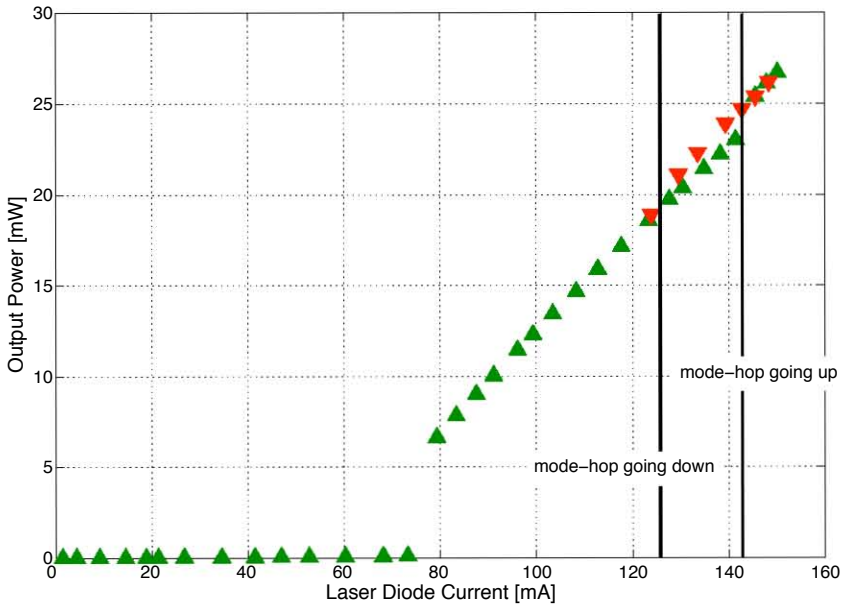

Figure 2.2: Plot of output power vs. drive current on the collimation diode. The location of the gain curve and the cavity modes shift at different rates with the drive current producing mode hops and hysteresis.

also affects the location of the peak of the gain curve with respect to wavelength and can thus be used as the medium frequency tuning mechanism. Again the electronics controlling the diodes are different: the collimation diode is set with a Thorlabs LDC 500 and the LM diode is set with a Newport 505 controller. Depending upon the temperature and humidity of the lab, the drive current required to produce the resonant wavelength drifts over time. While tuning the drive current, the cavity modes and gain curve shift at a different rate thus producing jumps between neighboring cavity modes. This has been examined primarily in the collimation diode [35] and results in both hysteresis and discontinuity in the power (Fig. 2.2) and wavelength (Fig. 2.3) tuning with respect to the diode drive current.

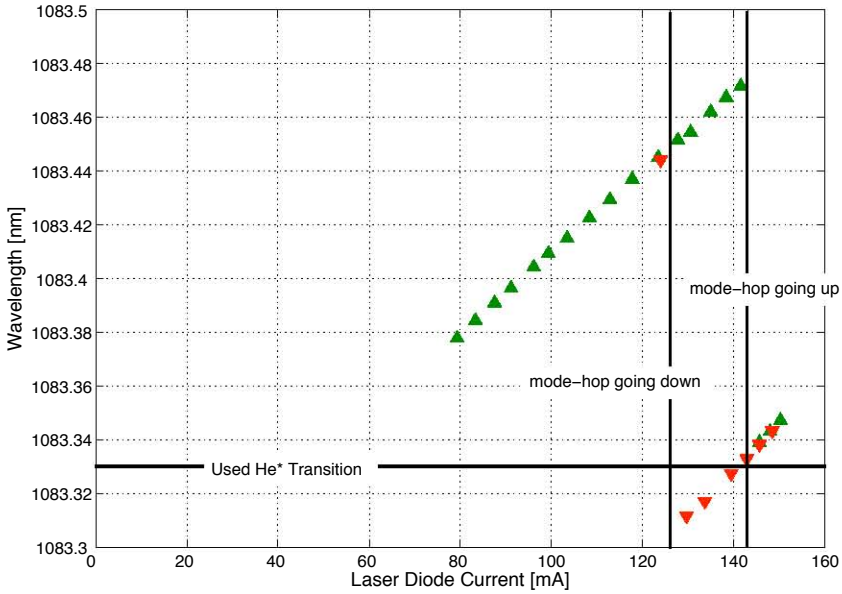

Figure 2.3: Plot of wavelength vs. drive current on the collimation diode. The location of the gain curve and the cavity modes shift at different rates with the drive current producing mode hops and hysteresis.

The external cavity (Fig. 2.1), in addition to performing the final narrowing of the output bandwidth, also serves as the diode's fine frequency tuning knob. It is the length of the cavity, controlled by the PZT on which the retro-reflecting mirror is mounted, that is ultimately used to set and hold the laser frequency (See Sec. 2.3). The PZT's for both diodes are driven by home built high voltage controllers.

2.2 Tailoring

2.2.1 Collimation Light

The collimation for the lithography experiment is done in four consecutive steps. The first collimation stage is accomplished using the bichromatic force [36–38]. This gathers a great deal of atoms and brings their transverse velocity to within the capture range of the three subsequent molasses stages: a high intensity booster molasses, a lower intensity Doppler molasses and an extra Doppler molasses. The first two molasses stages complete the collimation and the final molasses stage directs the atomic beam so that it is propagating exactly perpendicular to the LM. The light for these collimation stages is produced from the main beam of the collimation diode.

The collimation diode light, once launched into single mode fibers, produces two single frequency beams: one approximately 7 mW and one approximately 2 mW. The power in these beams is dependent on the coupling efficiency into the first fibers which periodically has to be tuned as a result of temperature and humidity swings in the lab. The 7 mW beam seeds the collimation system while the 2 mW beam is used to monitor the laser frequency for the first collimation alignment steps.

Bichromatic Light

The bichromatic force as described in section 1.4.2, at first glance does not present itself as a candidate for cooling. This is because the numerically calculated force profile shown in Fig. 1.9 is centered at $v = 0$. In order to use the force for collimation, the force profile must be shifted into the moving frame of

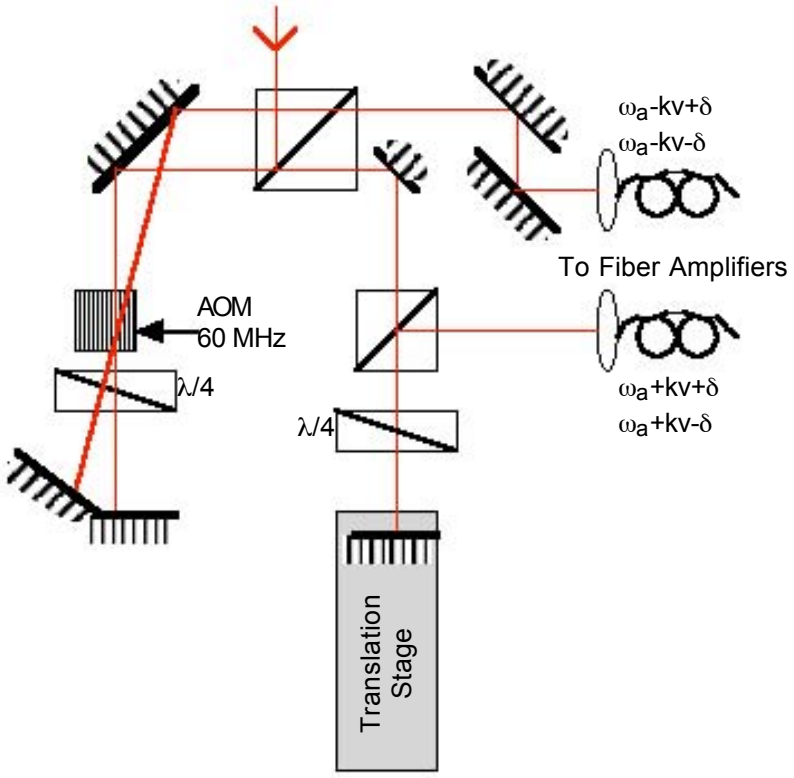

Figure 2.4: Double passing an AOM produces two beams with two frequencies. A moveable translation stage adjusts the relative phase between the two beams.

the atom such that it falls off at $v = 0$. In the lab frame this is accomplished by using two beams of amplitude modulated traveling waves where the carrier frequencies are Doppler detuned by $\pm kv$ to move the center velocity of the force profile. The two beams are created by double passing the 7 mW from the diode main beam fiber through an acousto-optic modulator (AOM) driven at a frequency $\frac{\delta}{2\pi}$ as shown in Fig. 2.4; with the result that one beam contains the spectral components $(\omega_{laser(l)}, \omega_l + 2\delta)$ which becomes the $+kv$ beam and the other beam contains the spectral components $(\omega_l \pm \delta)$ and becomes the $-kv$ beam. The AOM is driven at 60 MHz by an HP 3200B which is amplified

by a MiniCircuits ZHL-1-2W RF amplifier. For the bichromatic force this sets $\frac{\delta}{2\pi} = 60$ MHz, $\pm\frac{kv}{2\pi} = \pm 30$ MHz and the π-pulse length to 250 cm in the lab.

In order to establish directionality to the bichromatic force and insulate it from spontaneous emission effects, there must be a phase delay between the excitation pulse ($-kv$ light) and the emission pulse ($+kv$ light). A retro-reflecting delay stage (Fig. 2.4) on the $+kv$ light after the double passed AOM sets the phase between the counter propagating pulses such that the bichromatic force is maximized. This phase difference can be measured by observing the beat signal of two fast photodiodes measuring the bichromatic force beams; but given the limited accuracy of measuring the path length to the interaction region, the phase typically is set experimentally by maximizing the atomic peak from the bichromatic collimation.

Once the phase and the frequencies have been set, the two beams are launched into polarization maintaining fibers where they are either transported to Fabry-Perot cavities where the spectral content is monitored and adjusted by tilting the AOM and adjusting the drive power; or to the atomic collimation system.

For the bichromatic force to work with the detuning set by the AOM, each beam needs an intensity of $\sim 4000 s_o$ (Eq. 1.30). This is accomplished by seeding two Keyopsys Ytterbium(Yb)-doped fiber amplifiers, models KPS-BTQ-YFA-NLS-1083-40-COL, with the modulated light. Yb doped fiber has a broad absorption peak centered at 977 nm. The fiber can be pumped by commercially available high power diodes. This pump light, when injected through a V-groove in the outer cladding, propagates in the inner cladding causing a population inversion in the fiber and thus leading to amplification

of the injected seed light. These Keyopsys fiber amplifiers have three stages separated by optical isolators intended to prevent reverse lasing. The first stage of the amplifier is not variable and is supposed to be independent of the input power. It results in an initial output power of 100 mW. The following two stages are pumped by diode lasers whose current can be tuned to control the gain of the amplifiers. The current of the first diode can be turned up to 5 A and results in an output power of 3 W. The second diode at full power brings the output of the amplifier up to 4.3 W.

These fiber amplifiers saw first light for the bichromatic collimation experiment in January of 2004 and prior to that were rigorously tested for spontaneous Brillon scattering and other noise effects [37]. In order for the amplifiers to operate safely, they need to be seeded with at least -3 dBm (=0.5 mW) of light. Low input powers can result in amplified spontaneous emission, self lasing and ultimately catastrophic failure. For typical experimental runs, the input light is maintained above -1.5 dBm. If the input power is within the operating range, the output power is only slightly dependent on the input power.

Once the light is amplified, 650 mW of each amplifier is used for bichromatic collimation. In order to give the atoms an appreciable amount of time to interact with the bichromatic light, the amplified light is shaped by spherical and cylindrical telescopes. The resulting elliptical beam waists are 5.85 mm parallel to the atomic beam and 1.72 mm perpendicular to the atomic beam. These beams are chopped by an iris to be 11 mm long before they are sent to interact with the atoms. Due to the uni-directional nature of the shifted bichromatic force profile, four interaction regions are needed to achieve two

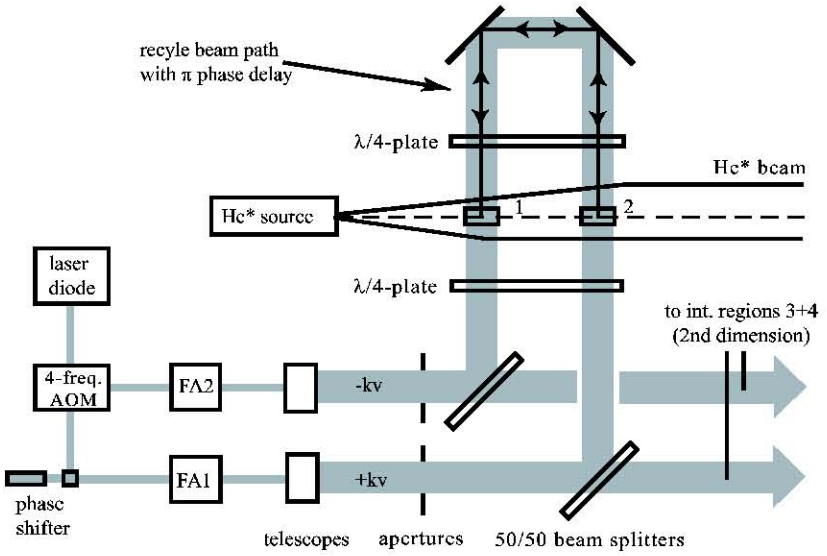

Figure 2.5: Four interaction regions are needed for two dimensional bichromatic collimation: two for each dimension.

dimensional atomic collimation: two for each dimension. In order to achieve this, the expanded beams are split by 50% beam splitters and then counter-propagated through the system (See Fig. 2.5).

In order to turn He* into a two level atom, the polarization of the light must be controlled. The plus- and minus- kv beams approach the system with orthogonal linear polarizations. These are set to within 1 part in 10^{-3} by polarization beam-splitting cubes (PBC's) before the expansion telescopes. The power into each polarization is roughly controlled by twisting the input fibers to the amplifiers and finely tuned by a controller on the amplifier which bends and twists an internal portion of fiber. The bi-refringence and polarization control in single mode fibers has been explored previously in this lab [35]. The bichromatic light is then circularly polarized by a $\lambda/4$ plate at the entrance to the atomic beam system, and then linearly polarized at the exit by another

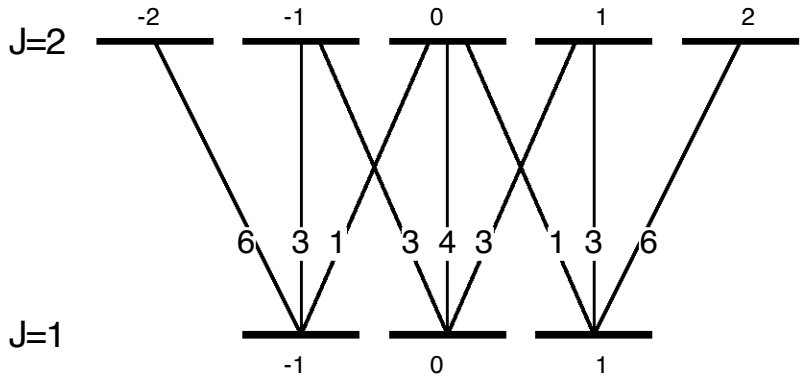

Figure 2.6: Transition strengths for various m_J and Δm_J values. The m=1 to m=2 transitions are the strongest and are driven by circularly polarized light.

$\lambda/4$ plate. This results that the plus and minus kv beams have the same helicity while they are interacting with the atoms. This polarization control forces the absorption to result in $\Delta m = +1$ and the stimulated emission to result in $\Delta m = -1$. Accounting for spontaneous emission, the atom is eventually pumped such that it is cycling on the $m = 1 \rightarrow m = 2$ sublevels, which is the strongest line for this transition (Fig. 2.6). In order to maintain the phase delay between the $+kv$ and $-kv$ beams; the beams are retro-reflected on each other such that there is a path difference of 125 cm between parallel interaction regions.

Molasses Light

The light for the three molasses stages is pulled off in two stages from the discarded polarization ("auxiliary line") out of the amplifier acting on the $-kv$ light. All of the molasses are effected using linearly polarized light. The linear polarization was chosen because, while in general the transition in He* is very strong, the $\Delta m = 0$ transitions are of similar strength and only half

as strong as the $\Delta m = \pm 1$ transition from the $m = \pm 1 \rightarrow m = \pm 2$ sublevels. Thus, with molasses needing significantly less light than the bichromatic force, it was it was experimentally easier to control the powers necessary for these collimation stages.

The booster molasses stage is a two dimensional molasses parallel to the orientation of the two dimensional bichromatic collimation. The light for this molasses is diverted from the auxiliary line of the $-kv$ light by an AOM that is tuned to 82 MHz. This AOM driven by a MiniCircuits ZOS-100 VCO that is amplified by a Minicircuits ZHL-03-5WF RF amplifier and results that one of the spectral components of the diverted then detuned $-kv$ light has a frequency $\omega_a - 5\gamma$. The detuned $-kv$ light is then sent through a single mode fiber in order to clean up the beam profile. The polarization of the light in this fiber is set by a Thorlabs FPC560 which, with a PBC in the light path, controls the power to the atoms. The original purpose of the PBC in this booster molasses line was for "piggy-backing" the light mask signal for amplification in a fiber amplifier [35] but with further examination, the spectral purity of light from the piggy-backing system was realized to be questionable. This molasses is typically aligned to maximize the atomic peak and is probably further detuned in the alignment process.

The light for the two Doppler molasses are diverted by an AOM tuned to 89 MHz. By virtue of the locking point for the collimation diode, which will be discussed below, this results that the $\omega_l - \delta$ light has a frequency of approximately $\omega_a - \gamma$; and that the other component of the light is so far off resonance that its action can be ignored. The AOM for this molasses is driven by an Isomet D301 B-856 AOM driver. This light is launched into a single

mode fiber that serves the dual purpose of producing lowest order Gaussian light for the collimation and controlling the polarization which controls the amount of light divided by a PBC and going either to the first Doppler molasses or the extra Doppler molasses.

The first Doppler molasses is a two dimensional molasses that is parallel to the orientation of the two dimensional bichomatic collimation. The beam for this molasses has waists of 4.4 mm parallel to the atomic beam and 1.45 mm perpendicular to the atomic beam; and a typical power of 3 mW which results in an $s_o = 10$. Just as with the booster molasses, this molasses is aligned in real-time to maximize the atomic peak and is probably further detuned in the process.

The extra Doppler molasses is a one dimensional molasses that operates horizontally (45° angle to the two dimensional collimation axis). It is expanded from the first molasses by a cylindrical telescope after the PBC that splits it off from the first Doppler molasses light. The beam for this molasses has waists of 4.4 mm parallel to the atomic beam and 3 mm perpendicular to the atomic beam, and a typical power of 0.180 mW which results in a peak $s_o = 2$. This molasses is aligned to the atomic beam and retro reflected at an angle smaller than 1 mrad.

Laser Lock Light

The light to lock the collimation diode is the final diversion out of the $-kv$ auxiliary line before the beam gets dumped. This light is diverted by an AOM tuned to 90MHz ($= \frac{3}{2}\frac{\delta}{2\pi}$) by a MiniCircuits ZOS-150 VCO that is amplified by a MiniCircuits ZHL-1-2W RF amplifier. This light is launched into a fiber

in order to transport it to the saturation absorption spectroscopy setup which will be described in Sec. 2.3. Eventually the collimation diode is locked such that $\omega_l = \omega_a - kv$ which properly sets the spectral components of the $\pm kv$ beams such that the center frequencies are $\omega_a + kv$ and $\omega_a - kv$ respectively.

2.2.2 Light Mask Beam

The laser tailoring for the light mask is currently much simpler than the collimation setup. The leakage beam out of LM diode is launched into a fiber for transportation to the saturation spectroscopy setup (Sec. 2.3) so that the laser frequency can be monitored. The fiber carrying the main beam is used to transport the light to an AOM detuning setup. This light is passed once through a Brimrose AOM that is driven at 490 MHz by an HP 3200B oscillator that is amplified by a home-built RF amplifier. The detuned light is then launched into an OptocomInnovation (previous name of Keyopsys) OIYb30 1W variable Yb-doped amplifier. This amplifier is the pre-curser to the amplifiers from Keyopsys that amplify the bichromatic light. It does not have the automatic security features (optical isolators, input power display) of the newer amplifiers and as a result can be a little more prone to failure and nonlinear reverse processes. The most common failure in recent years has been the destruction of the output fiber which is believed to be caused by external feedback into the amplifier.

The smaller amplifier allows us to set the LM power at anything up to 1W. The light exiting the amplifier comes to a waist of 400 μm, 86 cm away from the output coupler. There is a cylindrical telescope that expands the beam

in one dimension and is aligned such that the waist it produces lands on the spherical waist and is measured at 1400 μm.

2.3 Lock

2.3.1 Saturation Absorption Spectroscopy

Saturation absorption spectroscopy (SAS) is a standard technique that is used to compare a laser frequency to the energy levels of an atomic species [39]. For this experiment the atomic species, Helium, is contained in a glass cell. A discharge, produced by a strong RF field produced by an HP 8640B signal generator which oscillates at 52 MHz and amplified by an EIN 440 LA RF power amplifier, is used to create He^*.

The light directed to the SAS setup is split into three beams: two weak beams labeled the probe beam and reference beam and a strong beam labeled the pump beam (Fig. 2.7). This is accomplished by passing the incoming light through a thick glass plate. The probe and the reference beams are the reflections off the front and back surfaces of the plate and for the size of the setup are effectively parallel. When the probe and reference are co-propagated though the cell, light from both of these beams is absorbed by the atomic population. The absorption is Doppler broadened because of the different atomic velocities in the cell. The pump beam is passed around the cell and sent through it counter-propagating to the probe beam. The pump beam also excites atoms in its path and experiences Doppler broadened absorption. The stronger pump beam is more likely to interact with the atoms, thus if

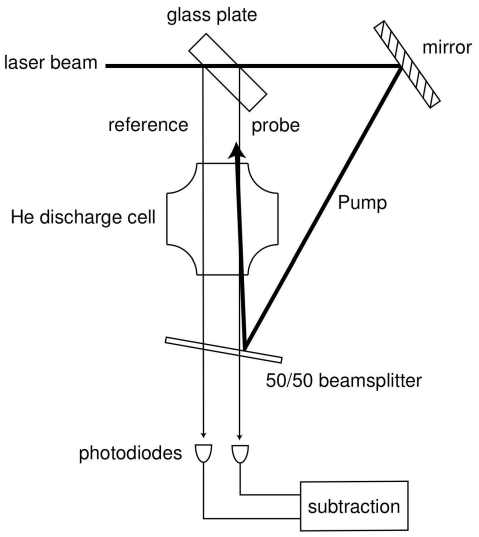

Figure 2.7: The spectrum of light absorbed from the reference beam by the atoms in the cell is Doppler broadened because of the different atomic velocities. The probe beam is not absorbed by atoms that are resonant with both it and the pump beam.

the atoms are resonant with both the pump and the probe beam (the atomic velocity component parallel to the laser propagation is 0 m/s) they are more likely to absorb from the pump beam and not the probe beam. This creates a dip in the absorption signal of the probe beam. Subtracting the absorption signal of the reference beam leaves the Doppler free absorption peak (Fig. 2.8).

In the event there are multiple atomic levels or multiple laser frequencies so-called cross-over peaks are observed. In the case of multiple addressable atomic levels, this is caused by the velocity distribution bringing one level to resonance in the probe beam and a different level to resonance at the same time in the pump beam. These peaks are larger than the single level peaks because they involve two different atomic populations.

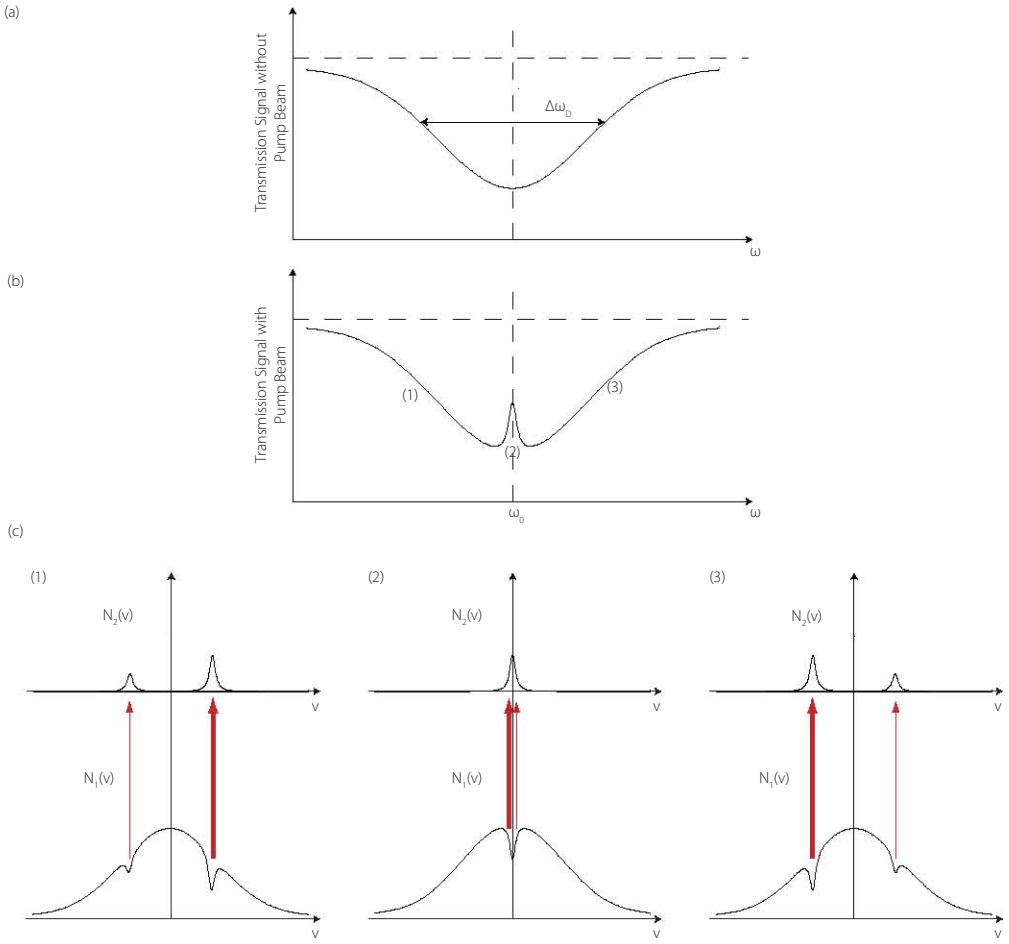

Figure 2.8:
(a) In the transmission signal without the pump beam the atomic transition is Doppler broadened.
(b) When the pump beam is present, a small Doppler free signal can be seen on top of the broad dip due to saturation effects.
(c) Only if the laser is resonant with the atomic transition the pump beam and the probe beam talk to the same velocity group of atoms $v_{\parallel} \approx 0$. That leads to a higher transmission of the probe beam since the stronger pump beam saturates the absorption of that velocity group.

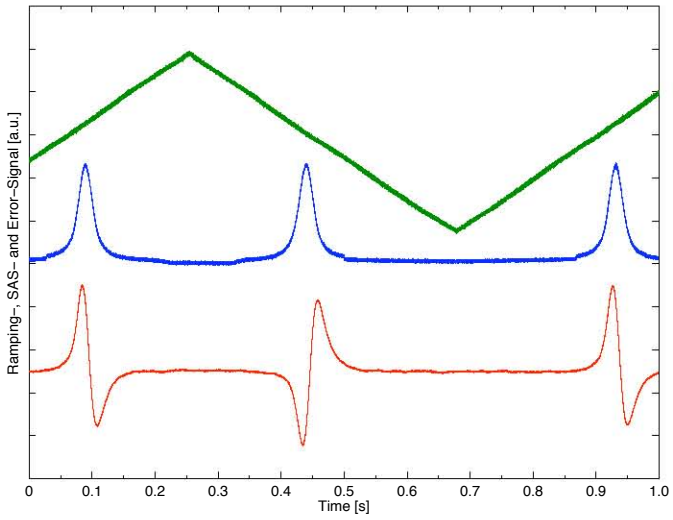

Figure 2.9: The figure shows the SAS signal (blue) and the arising error signal (red) for the first locking scheme. The frequency of the ramping (green) is slowed down to ~ 1 Hz to display the error signal more accurately on the oscilloscope. Usually the scanning frequency is ~ 30 Hz.

2.3.2 Locking Electronics

In order to lock the laser, an error signal must be created from the Doppler free transition signal of SAS and then fed back to the laser control (Fig. 2.9). The electronics on the collimation lock and the LM lock are slightly different, but the procedure is the same.

The error signal for the lock is created by adding a small high frequency dither to the laser frequency through its drive current. The resulting SAS signal with the dither impressed on it is fed into a lock-in amplifier which effectively takes the derivative of the input signal by multiplying it with a sine wave at the same frequency as the dither and sending the result through a low-pass filter. The error signal is connected to a proportional-integral-derivative

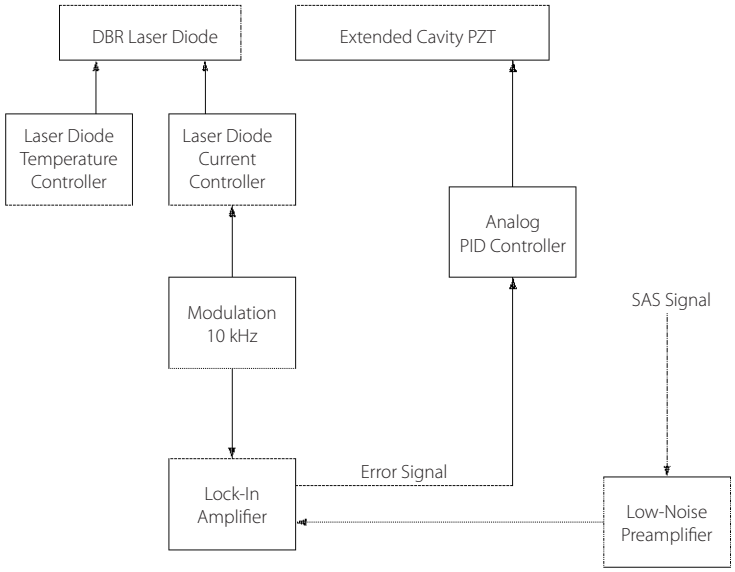

Figure 2.10: Schematics of the locking electronics. Details about the components can be found in the text.

(PID) controller whose output is fed, through home-made electronics, to the high-voltage amplifier controlling the PZT on the external cavity of the diode laser. As the laser drifts off resonance, the cavity length is adjusted to bring it back (Fig. 2.10).

Collimation Lock

For the collimation diode, the Doppler free SAS signal is amplified and filtered with a Stanford Research Systems (SRS) SR560 low-noise preamplifier. The lock-in amplifier is a EG&G Princeton Applied Research model 5104 that is triggered at 10 kHz by an SRS DS345 30MHz synthesized function generator that also provides the dither signal for the laser diode current. The PID controller is an analog SRS SIM960. In the absence of severe acoustic (slamming

doors) or electrical (there is sometimes evidence of ground loop) noise the laser can remain locked for several hours.

Light Mask Lock

The Doppler Free SAS signal from the Light Mask diode is amplified by a Princeton Advanced Research model 126 lock-in amplifier. The 10 kHz laser current dither is accomplished with the internal oscillator of the lock-in amplifier. The resulting error signal is stabilized by another analog SRS SIM960 PID controller. The error signal from this lock tends to drift a little further than that of the collimation diode lock, but as it drifts, it is less likely to jump away from the lock point.

Chapter 3

Metastable Helium Beam

Previous research efforts in our laboratory have been dedicated to the production and control of a bright metastable 2^3S_1 Helium (He*) beam [29, 37, 38]. This chapter serves to summarize some of this previous work and describe the additions to the He* beam apparatus to make it suitable for the atomic lithography experiments.

3.1 Vacuum System

The vacuum system is composed of standard 4" diameter stainless steel parts connected primarily with copper gasket sealed Conflat flanges. Theoretically this system should pump well into the ultra high vacuum regime; but in practice the constant opening for lithography, the existence of some O-ring sealed connections, and some internal components not designed for UHV systems raise the typical resting pressure to approximately 10^{-7} Torr.

A diagram of the vacuum system is presented in Figure 3.1. The system is

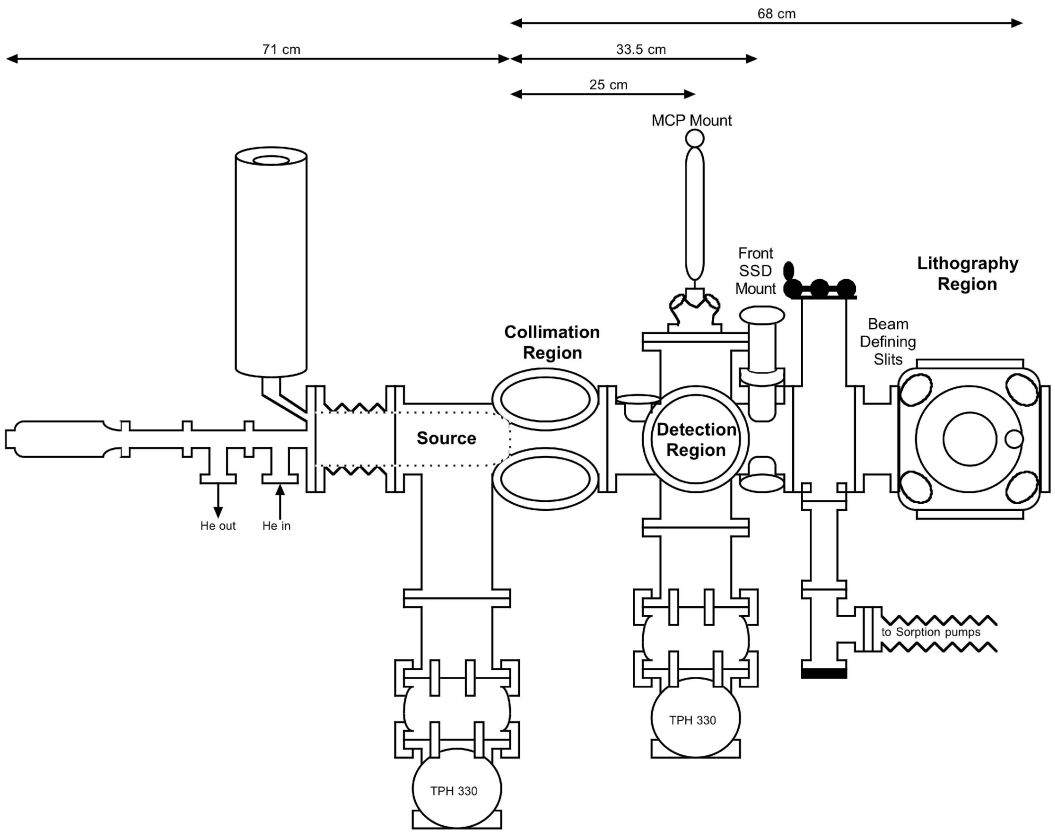

Figure 3.1: The system has two differentially pumped chambers, the source and beam chamber, separated by a wall with a 3 mm diameter aperture. The lithography region can be isolated from the rest of the system by a gate valve to facilitate easy loading of the samples. The typical resting pressure of the system is approximately 5×10^{-7} Torr.

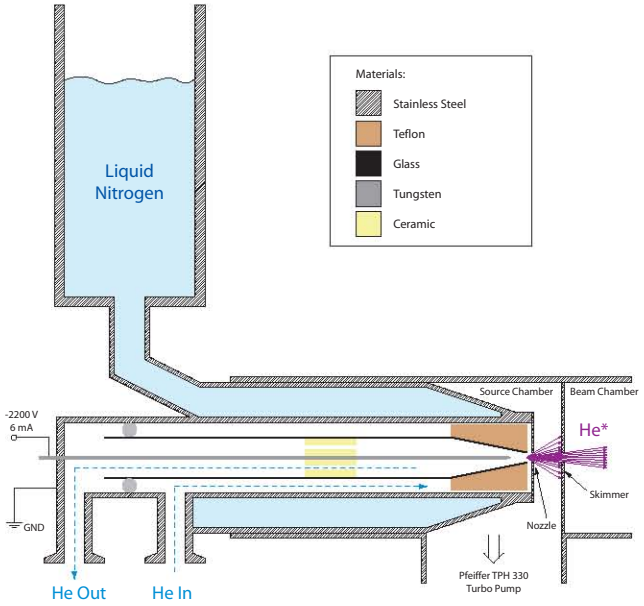

Figure 3.2: He flows in around the outside of the glass tube to the discharge region. Most of the He is pumped out through the glass tube. He* is created by recombination after the discharge region.

divided into the source and and beam chambers. These chambers are separated by a wall with a 3 mm diameter aperture so they are differentially pumped. The beam chamber can be further broken down into the collimation region, detection region and lithography region.

3.1.1 Helium Source

Because of the doubly-disallowed nature and large energy gap of the of the $1^1S_0 \rightarrow 2^3S_1$ transition, which is discussed in Sec. 1.5, metastables are most effectively produced in a discharge. In this atomic beam, He* is produced by a reverse flow DC discharge source designed by Kawanaka et. al. [40] and modified by Mastwijk et al. [41]. Two of these sources are currently in

operation in our laboratory. The source for the present experiment was built by the machine shop at Universiteit Utrecht (Netherlands). It was assembled in 1998 and was producing a stable He* beam by 1999 [29].

In the reverse flow design (Fig. 3.2), Helium is flowed into the source between the outside of a 1 cm diameter glass tube and a 3 cm diameter stainless steel jacket that is cooled by liquid Nitrogen to 77 K. The glass tube narrows at the end and is centered inside the steel jacket by a teflon spacer. Helium is forced around the outside of this spacer and brought into closer contact with the steel jacket so that the gas has been cooled considerably by the time it reaches the discharge region. Most of the He is pumped out through the glass tube by a Welch 1376 rotary vane mechanical pump. Inside the glass tube is a needle made from a 1 mm diameter Tungsten welding rod that has been sharpened to a point and is centered in the glass tube by a teflon spacer with areas cut out to allow proper gas flow by it. For the correct operation of the source the rod must be pure tungsten and the sharpening must be done with fine sand paper such that the grooves in the sharpened point run parallel to the length of the rod. The end of the steel jacket housing the glass tube is closed by a piece of Aluminum with a 0.5 mm diameter aperture (nozzle plate). The Tungsten needle is mounted on a linear motion feedthrough that allows the distance between the end of the needle and the nozzle plate to be adjusted. With the Tungsten needle held at a high negative voltage by an HP 6525A DC Power Supply through a 170 kΩ chain of high power resistors (-2500 V results in a current of 6 mA), a discharge is lit between it and the nozzle plate.

In the plasma produced by the discharge between the needle and the nozzle plate Helium is present in its ionic form and various excited states. Most of the

He* that is produced inside the plasma is quenched by the high pressure in the region. The bulk of the He* production from the source occurs in the region between the nozzle plate and the skimmer, which is a 3 mm diameter aperture on a plate attached to the wall separating the source chamber from the beam chamber. In this area, He* is created by collisions with secondary electrons and by recombination of He^+ with electrons. The He* along with charged particles, UV light and ground state He escape from this region through the skimmer into the beam chamber.

The parameters which result in stable operation of the source are due primarily to the gas flow through the source and are thus dependent on the geometry of the chamber in which the source is housed, the gas flow lines, and on the quality of the vacuum attainable by the available pumps. The construction of the source and adjoining collimation chamber are described in [38]. The source chamber consists of a 4" diameter stainless steel "T" with two 6" Conflat flanges and a wall containing a bore for a skimmer plate. The source is attached to the chamber by a bellows piece which allows for alignment of the nozzle aperture to the skimmer aperture. Directly above the skimmer plate wall there is a 0.75" diameter tube with a 1.33" Conflat viewport. This allows us to monitor the color and brightness of the discharge between the nozzle and skimmer plates. The chamber is pumped by a Pfeiffer TPH 330 turbo pump which is backed by a Pfeiffer DUO 10 PK D62 707 B mechanical pump. The resting pressure of the chamber, measured by an ion gauge read by a Veeco Instruments Model RG-830 gauge controller, is typically 9×10^{-7} Torr.

The gas flow into the source is controlled by a needle valve on the inlet.

This is set such that when the He gas is flowing through the cooled source the pressure on the inlet is too high for the gauge to read, the pressure at the outlet of the glass tube is 1 Torr and the backing pressure on the source pump is 178 ± 3 mTorr. All of these pressures are measured by Granville-Phillips Convectron gauges and read by Terranova Scientific Model 926 Gauge Controllers.

The discharge will run stably at currents from 2 mA up to 12 mA. The higher currents, while producing more He*, result in "hotter" discharges that produce atoms with larger longitudinal velocities. In addition, higher currents accelerate the carbonaceous build up on the inside of the glass tube from the discharge. This requires the source to be cleaned more often. Typically the source is run at 6 mA as a trade-off between He* production and beam velocity.

3.1.2 Collimation Region

Welded to the end of the source chamber is a short arm six-way cross with 6" Conflat ports. The four arms of the cross that are perpendicular to the axis of the beam line are at a 45 deg angle to the vertical axis. These ports have 6" Conflat flanges and are sealed by 4" windows that have been anti-reflection (AR) coated for both λ =1083 nm and λ =389 nm light. Asymmetric Helmholtz coils wrapped around the center beam on either side of the access windows create a magnetic field to cancel the component of the Earth's magnetic field along the beam line. It is in this 4" region that the bulk of the atomic collimation is achieved with the bichromatic force and first two molasses stages.

3.1.3 Detection Region

The next region down the line houses the detectors required for alignment and calibration of the atomic beam. It is another six-way cross primarily with 6" Conflat flanges. This chamber was adapted from the original source chamber, a four-way cross, for the bichromatic slowing experiments [29] and still contains the wall for the skimmer plate mount. The original chamber was converted into a six-way cross in order to gain more optical access to the atomic beam and to monitor it in real-time on the Micro Channel Plate - Phosphor Screen detector (MCP-Ph.Sc.) which is discussed in Sec. 3.2.1. The top port of the cross is dedicated to the MCP-Phosphor Screen mount and control electronics. The bottom port is for the Pfeiffer TPH 330 that pumps the beam chamber. This turbo pump is backed by an Alcatel 2008A mechanical pump and the foreline pressure is monitored by a Granville-Phillips Convectron gauge that is read by a Terranova Scientific Model 926 Gauge Controller.

When the two extra 4" diameter tubes were added to make the chamber into a six-way cross, the welder advised that the structure would buckle if 4" diameter holes were bored and then welded; thus, the two horizontal ports which hold windows originate from the body of the cross with 3.5" diameter stainless steel tubing and then there is an abrupt step out to 4" diameter tubing to hold the 6" Conflat flange. This somewhat limits the optical access into the cross at this point. These ports are sealed with 4" windows that have also been AR coated for both λ =1083 nm and λ =389 nm light and mounted on 6" Conflat flanges.

In addition to the six 6" Conflat ports, there are five additional 2.75"

Conflat access ports. The first one provides the electrical access for a pair of steel plates held at +1000 V that are used to sweep the charged particles out of the beam. These plates sit between the optical access provided in the collimation region and the detection region. The other four 2.75" Conflat access ports sit after the horizontal optical access described previously. These ports are oriented parallel to the collimation windows closer to the source and at a 45^o angle to the optical access provided by the newer ports. They support an ion gauge and crossed stainless steel plate detectors (SSD) and the electrical connections to monitor the absolute current of the atomic beam (see Sec. 3.2.2).

3.1.4 Lithography Region

The lithography region consists of a 6" Conflat "Spherical Cube" (Part # MCF600-ESC600800) from Kimball Physics. This chamber has six 6" Conflat ports and eight 2.75" Conflat ports corresponding to six faces and eight corners of a cube. This region can be isolated from the rest of the beam line by a TLG4000-100-21(600400)-1102 gate valve from Thermionics that has a 2.75" Conflat roughing port on the bottom. The roughing port is connected to two sorption pumps and a dry Nitrogen tank to facilitate the frequent cycling of this chamber.

The chamber is oriented such that the 6" Conflat ports are in the horizontal and vertical plane. The two horizontal ports perpendicular to the direction of the atomic beam are sealed by NorCal ADV-600 Quick Access Doors. These are 6" Conflat flanges with a 3.5" window (AR coated for λ =1083 nm and

λ =389 nm light) on a hinge that are O-ring sealed for the vacuum. These doors facilitate easy transfer of the detection equipment and lithography samples.

Only five of the eight 2.75" Conflat ports are in use, the rest are sealed with blank flanges. The front top two ports are used to mount a horizontal and vertical slit respectively. The vertical slit also has a 1 mm periodic Copper mesh mounted in it. These slits and the mesh serve to define the atomic beam and prevent charged particles present in the beam line after the deflection plates from influencing the exposure. The other three 2.75" ports in use are dedicated to electrical connections for the detection and exposure positioning equipment and a residual gas analyzer which is periodically used to troubleshoot and monitor the quality of the vacuum.

The back 6" Conflat port of the lithography chamber is used to mount a two axis motorized stage from National Aperture. The stage is contained in the 4" diameter area of the open port and it has a 1.5" range of motion along each axis. There are several identically machined mounts to attach to the stage. One is permanently in the vacuum system and holds a SSD that is used to monitor the beam where the lithography exposures occur and the others have been used for various incarnations of the lithography sample mount (Sec. 4.3). The stage is controlled from the computer by a program that was written in 2005 and is discussed in [35].

3.2 Metastable Helium Detection

The 20 eV of internal energy carried by He* makes it relatively easy to detect. This is because He* will decay to the ground state of He upon colliding with a surface. This decay releases the internal energy which is enough to eject an electron from most surfaces. Realtime linear detectors are needed for the alignment and measurement of the He* beam. We do not have a detector that fulfills both requirements, but we have two types of detectors that together fulfill the measurement requirements.

3.2.1 Micro-channel Plate and Phosphor Screen

A micro-channel plate (MCP) and Phosphor screen (Ph.Sc.) detector when imaged by a camera serve the purpose of giving real time qualitative measurements of the atomic beam. This detector has a non-linear response to the He* and shows aging over time. Regardless, it is indispensable for the alignment and trouble shooting of the atomic collimation.

An MCP is a set of 10 μm to 100 μm diameter tubes acting as continuous dynode structures. These tubes typically have semi-conducting walls which have also been treated to promote secondary electron emission. They are fabricated into a glass plate using a glass drawing technique similar to that for optical fiber production. Parallel electrical contact between the ends of the tubes is established with a conducting metallic coating on the surface. The electrical properties of the plate tend to depend highly on the length to diameter ratio of the tubes with the typical resistance between the surfaces being on the order of 10^9 Ω. The plates must be operated under a vacuum of at

least 10^{-5} Torr and need to be stored in a dry environment (preferably under vacuum) or else they crack. When He* strikes the plate it decays to the ground state of He and ejects an electron into one of the channels. The potential difference between the surfaces of the plate determine the amplification, typically several orders of magnitude, of that electron.

The MCP's in use in this experiment were purchased from Burle Electro-Optics. The channel diameters are 10 μm with a center to center spacing of 12 μm. They have a bias angle of 12^o and a length to diameter ration of 40:1. The active area has a diameter of 25 mm and the plates can take a maximum of 1000 V.

The Ph.Sc. is a glass substrate with a thin coating of Indium Tin Oxide (ITO) covered by a coating of P43 Phosphor. The ITO serves to diffuse charge buildup on the plate during operation. Around the edge of the plate is a ring of Aluminum that helps the electrical connection to the ITO so that charge can be drained away. The Ph.Sc. used in this experiment was purchased from Lexel Imaging Systems and the active area has a diameter of 25 mm.

The MCP and Ph.Sc. are mounted 0.05" from each other in standard Kimball Physics eV parts on a 4" Huntington linear motion feedthrough. The detector monitors the beam 25 cm from the skimmer plate. In order to multiply the electrons in the MCP, the front plate is held at -500 V and the back plate is grounded to the outside of the vacuum system. A potential of +1500 V is put on the front of the Ph.Sc. to accelerate the electrons from the MCP and then drain them off after they have caused the Phosphor to fluoresce. As the end of the vacuum system is blocked by the lithography positioning stage, the image on the phosphor screen is viewed on a mirror mounted at 45^o on the

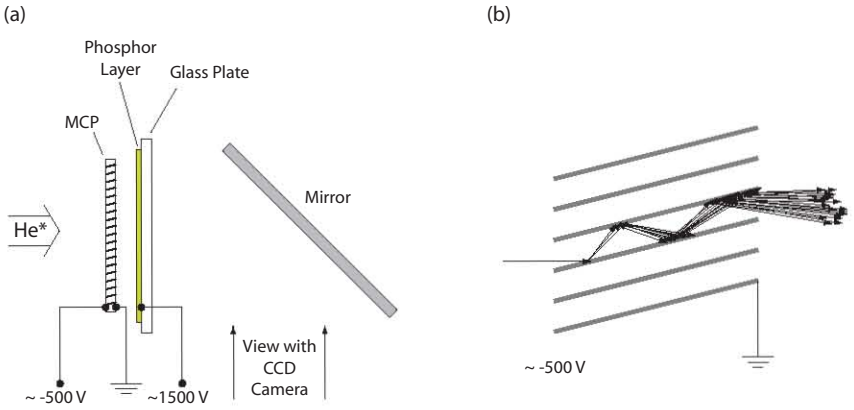

Figure 3.3: (a) Arrangement of the microchannel plate and phosphor screen as seen from the top. The mirror is inserted to be able to detect the phosphor screen image through a window at the side of the vacuum system.
(b) Principle of electron multiplication within a microchannel plate. The incoming He* atom knocks out the first electron that gets accelerated by the high voltage difference and creates large numbers of secondary electrons in electron-wall collisions within the microchannels..

back of the MCP-Ph.Sc. detector (Fig. 3.3). Bitmap images are acquired by a CCD camera and are analyzed in ImageJ, a public domain Java application developed by the National Institutes of Health.

3.2.2 Stainless Steel Plate Detector

The two stainless steel plate detectors (SSD) provide a linear measurement of the atomic flux. These detectors are essentially cheap, home made Faraday cups consisting of two parallel steel plates electrically isolated from each other. The front plate has an aperture in it and is held at a positive potential with respect to the back plate which is connected through a Kiethly 486 picoammeter to ground. When a He* atom lands on a steel plate, there is a 70% chance that it will eject an electron [42]. With the SSD setup, if the electron is ejected

from the grounded plate it is drawn towards the high potential inducing a current up from ground. Electrons ejected from the higher potential plate are just attracted back to it. The resulting current from ground is dependent on the size of the aperture and can be converted into a He* flux measurement.

$$\underset{\text{Flux}}{\text{He}^*} = \underset{\text{current}}{\text{picoammeter}} \left[10^{-12}\frac{\text{C}}{\text{s}}\right] \frac{1\ \text{e}^-}{1.6\cdot 10^{-19}\ \text{C}} \frac{1\ \text{He}^*}{0.7\ \text{e}^-} \frac{1}{\text{area of aperture}} \quad (3.1)$$

The front SSD (Fig. 3.4) is mounted just behind the MCP-Ph.Sc. detector 33.5 cm from the skimmer plate. The SSD is comprised of two pieces, one in front of the other, each mounted on a separate Huntington manual linear motion vacuum feed-through. These feed-throughs are perpendicular to each other and parallel to the collimation axes. The front piece is a plate with a slit 37 mm long and 0.205 mm wide that is held at +250 V. The second piece has a smaller wider slit (58 mm long and 0.5 mm wide) also held at +250 V and a back plate that is grounded through the pico-ammeter. The resulting SSD has an aperture of 0.2 mm^2 and two dimensional positioning abilities. The manual positioning system for this SSD makes two dimensional mapping of the beam time consuming, but it is more sensitive than the second SSD to the individual collimation stages and is thus mostly used as a diagnostic tool.

The back SSD (Fig. 3.5) is a monolithic piece (front plate with an 0.456 mm diameter aperture and back plate) mounted on the stage at the back of the vacuum system. The positioning and measurement from this SSD is fully automated and incorporated into the stage control program. This is accomplished by amplifying the pico-ammeter readout with an Ithaco 1201 low-noise pre-amplifier and then recording it into the computer with a Ni USB-

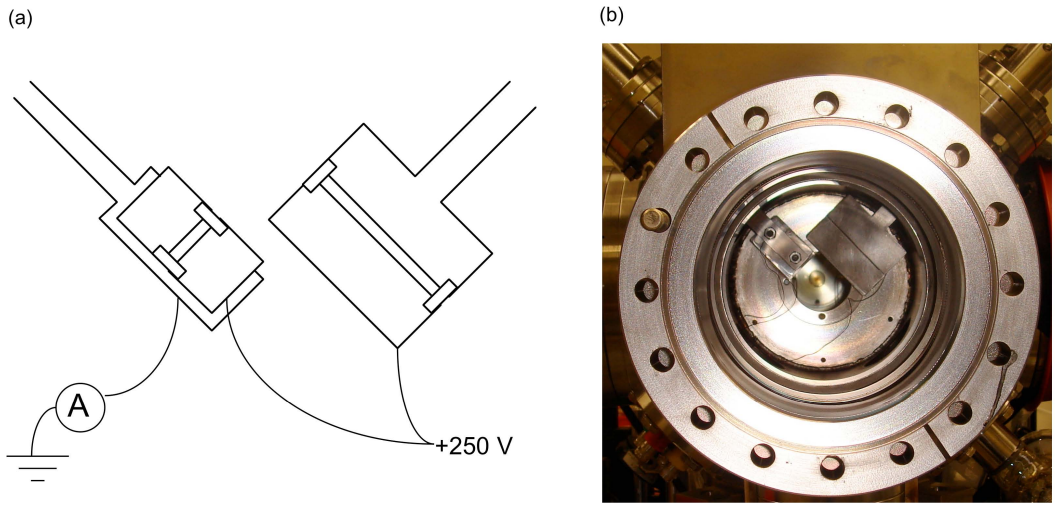

Figure 3.4: (a) Schematic of the front SSD's. The longer slit crosses in front of the shorter one making a square aperture. He* ejects electrons off the back plate inducing a current up from ground measured by a pico ammeter.
(b) Photograph of the back of the front SSD's.

6008 data acquisition box. This SSD is used to scan the beam daily in order to find the optimal location for the lithography exposures.

3.3 Collimation Procedure

The He* source on the experiment is operated between the effusive and supersonic regimes. While this results in slight collimation and directionality in the source output it does not result in a beam that can be used for lithography: the transverse velocity distribution is too wide and the atomic dosage in the lithography chamber is not large enough to result in exposures that are less than several hours long. The collimation procedure developed in this lab [36–38] and further modified for the lithography experiment results in a He* beam bright enough to keep the lithography exposure under an hour and with a low

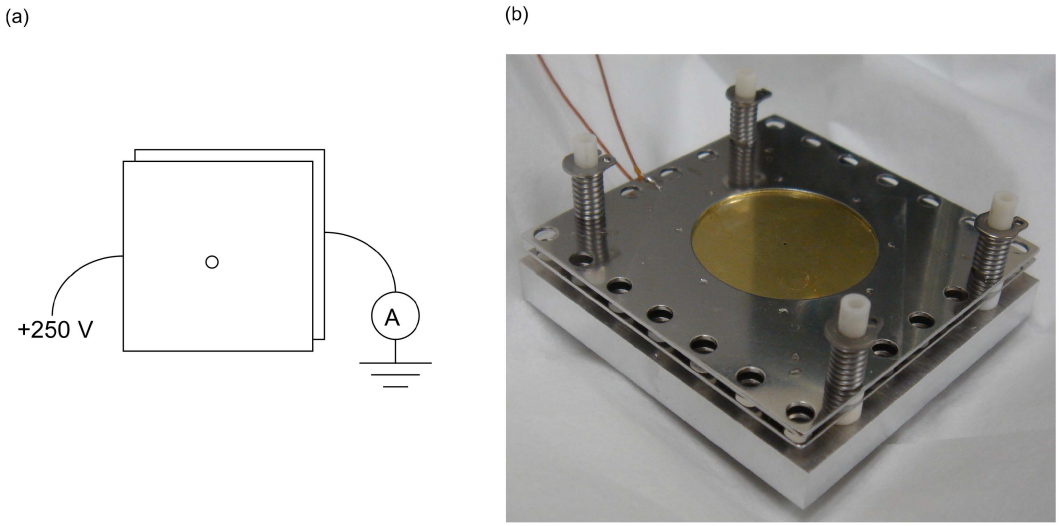

Figure 3.5: (a) Schematic of the back SSD's.
(b) Photograph of the back SSD outside of the vacuum system.

enough transverse velocity spread to use an optical mask for patterning.

3.3.1 Bichromatic Collimation

As described in Sec. 2.2.1, for the bichromatic force to be used for two dimensional collimation, there need to be four interaction regions: two for each dimension. Each interaction region is approximately 10 mm long and has approximately 2 mm of clearance on each side. The collimation light is aligned by setting the frequency of the seed diode to the transition resonance. This brings one of the components of the $+kv$ light to atomic resonance. When the $+kv$ light is attenuated, the radiative force on the atoms is seen on the MCP-Ph.Sc. detector. The radiative push from the first and third interaction regions are then centered on each other and the $-kv$ light is aligned through the vacuum system parallel to the $+kv$ light. The beams are then reflected

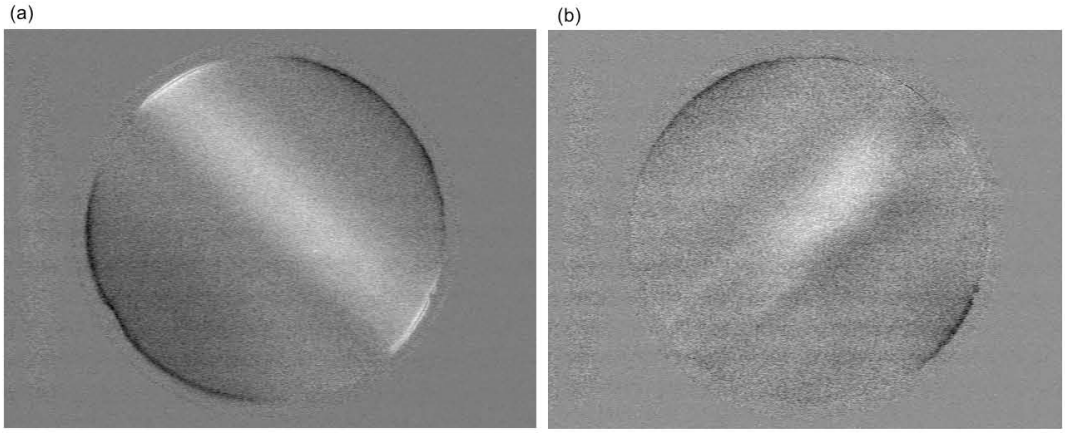

Figure 3.6: MCP-Ph.Sc. pictures of each dimension of bichromatic collimation. (a) The first dimension appears longer than the second dimension because its action is closer to the skimmer.
(b) The edges of the second dimension show other high intensity molasses effects.

back on each other. The quality of the bichromatic collimation is first analyzed on the MCP/PhSc detector, looking at each dimension separately (Fig. 3.6). The bichromatic collimation brings the divergence of the atomic beam down to 10 mrad and results in a peak of 18-23 pA at the front SSD.

3.3.2 Molasses Collimation

The Booster molasses and Doppler molasses two dimensional collimation stages are aligned to the peak of the bichromatic collimation as viewed on the MCP-Ph.Sc. detector. These two collimation stages bring the divergence of the atomic beam down to 1.1 mrad in the horizontal and 3.14 mrad in the vertical. It is these two collimation stages that result in the nicely defined 3 mm diameter atomic beam in the lithography chamber (Fig. 3.7) with a peak of 1.5×10^9 atoms/mm^{2}s, 70 cm from the skimmer.

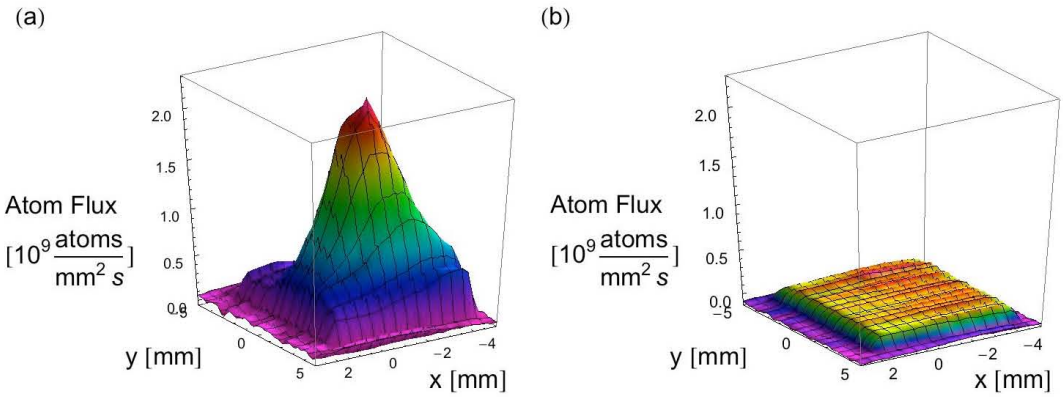

Figure 3.7: Back SSD scan of the full collimation. (a) Peak Scan. (b) Background Scan.

The main purpose of the extra one dimensional Doppler molasses is to make sure that the atomic beam arrives at the lithography chamber perpendicular to the light mask beam. The action of this collimation stage is too far down the beam line to be detected by the MCP-Ph.Sc. This molasses is aligned to be parallel to the light mask beam, which is aligned visually to the final detector when it is sitting at the atomic peak, and then exactly retro-reflected on itself at an angle smaller than 1 mrad. This molasses does not typically greatly effect the intensity of the atomic beam as measured in the lithography chamber.

Chapter 4

Lithography Process

For the direct deposition fabrication experiments very little sample preparation beyond standard cleaning is required. For resist-assisted lithography, sample preparation and handling is a critical factor in the success of the experiment. The resist protects the gold layer against a wet chemical etch. During the experiment it is destroyed by the 20 eV of internal energy carried by the He^* atoms. If there is further destruction to the resist or if the resist is formed with too many defects, the pattern created by the He^* atoms is washed out. Even with careful standardization of pre and post exposure processes, the repetition of experimental results is challenging.

For these experiments the sample preparation is completed with a combination of external and in-house procedures. All the sample handling and analysis in our lab is done in a laminar flow station that is also equipped with a fume hood.

Diameter	2” (50.8 mm)
Grade	Prime
Surface Finish Front	Polished
Surface Finish Back	Etched
Growth Method	Cz
Orientation	$\langle 100 \rangle$
Resistivity	1-20 Ω cm
Thickness	250-300 μm
Coating	50 Å Cr / 200 Å Au, evaporated

Table 4.1: Commercial specifications of the silicon wafers used as sample substrate.

4.1 Wafers and Coating

The wafers used in the experiment are 2” diameter silicon wafers supplied by Montco Silicon Technologies. Montco Silicon Technologies grows the wafers, cleans them using the industry standard RCA-1 cleaning process, polishes them, and then outsources the coating process to Scientific Coatings. The wafers are coated in an e-beam evaporator with a 50 Å Chromium adhesion promotion layer and then a 200 Å Gold (Au) layer. The specifications of the wafer can be found in Table 4.1.

The quality of the Au substrate affects the rest of the experimental process and currently, along with the etching process (Sec. 4.4), limits the achievable resolution. The current coating is just thick enough to provide uniform coverage of the wafers. Au, when evaporated onto a wafer, undergoes island growth building up in small grains similar to water evaporating onto a smooth surface. The resulting coating is not atomically smooth, but has a granularity on the order of 10’s of nm with a typical RMS surface roughness of a few nm. The granularity and surface roughness are directly effected by the underlying sub-

strate, deposition temperature, deposition rate and post deposition annealing [43]. As the experiment proceeds in the future, more care will have to be taken with the substrate deposition process.

Once the wafers have arrived in our lab they are diced into 4 mm by 12 mm samples by a neighboring lab. Wafers can be diced by applying pressure with a sharp edge, but this method results in significant damage to the Au coating along the edges of the break. In order to minimize this damage during dicing, a coat of Microposit S1813 Photo Resist is spun onto the wafer. The wafer is mounted on a sheet of 3M blue tape and then cleaved by a diamond-and-epoxy resin blade in a Model 1006 Micro Automation programmable dicing saw. In this process, the saw cuts through about 2/3 of the wafer thickness leaving about 100 nm uncut. The entire wafer is diced at once and then the 4 mm by 12 mm pieces are easily broken away from the wafer as needed in the experiment.

4.2 Resist Formation

Once the wafers have been diced, they must be cleaned and the gold re-exposed before another resist can be deposited. There are several cleaning methods available; we achieve the most repeatable results with the process in Table 4.2. The acetone serves to remove the S1813 protective photo resist. The ethanol rinses away the acetone and any oxidization making it safe to allow the wafer to sit in the Piranha solution (75 % Sulfuric Acid, 25 % Hydrogen Peroxide; very dangerous mixture handled with care under the fume hood). The Piranha solution dissolves any organic material on the Au surface. After

Acetone	Ultra Sonic Cleaner	10 min
Ethanol	Ultra Sonic Cleaner	10 min
Piranha Solution	Bath	10 min
Ethanol	Rinse	—-

Table 4.2: Before the Au coated Si wafers are coated with the alkanethiol resist, they must be cleaned.

the 10 min Piranha bath, the wafer is rinsed again with ethanol to remove any Piranha residues.

The formation of Self Assembled Monolayers (SAM) of thiols on surfaces is an extensive field of research by itself [44]. Alkanethiols are a class of amphiphilic molecules with a hydrophilic Sulfur head group and a hydrophobic Methane group attached to the end of a long hydrocarbon chain. The most common resist for atomic lithography with an Au substrate is nonanethiol with eight CH_2 elements in the chain and the Sulfur head group and Methane tail group.

In order to create the SAM resist on the Au surface of the Si wafer, the wafer is submerged in a 1 mM solution of Nonanethiol (Sigma-Aldrich, 1-Nonanethiol, technical $\geqq$99%) in ethanol (200 proof, ACS/USP grade, Pharmco Products Inc.) for 13 to 20 hours. We find this gives repeatable lithography results even though the literature indicates that the initial uptake of the thiol onto the Au surface happens in a few minutes and results in 80 to 90 % of the coverage. The SAM initially forms in islands across the wafer as the sulfur head groups undergo chemisorption and the carbon chains lie flat on the Au surface. As more molecules are taken up, the hydrocarbon chains are straightened and lift off the surface. Finally, there is a reorientation of the terminal groups as the molecules become closely packed. The resulting SAM has a

$(\sqrt{3} \times \sqrt{3})$R30^o lattice structure with the hydrocarbon chains tilted 32^o - 35^o from the normal of the sample in an all trans orientation that is rotated 55^o from the plane established by the chain tilt and substrate normal.

The damage caused to the SAM by the 20 eV of internal energy from the He* atoms is not very well understood. It is suggested that the internal energy of the He* atoms causes the hydrocarbon chain in one molecule to break and release secondary electrons that weaken or destroy the neighboring molecules [45, 46], thus destroying the hydrophobicity of the damaged molecule and leaving the underlying layer suceptible to the etch (Sec. 4.4).

4.3 Sample Mounts and Exposure Process

The sample mount and exposure process have evolved dramatically as a part of the work presented in this dissertation. When the process of mounting the sample in the atomic beam for the exposure was disrupted, typically by difficulty with the mount, it seemed to result in severe damage to the resist and subsequently unsuccessful experimental runs. This indicated the necessity of a mount that easily accepted that sample and then was simple to load into the atomic beam.

The original atomic beam apparatus did not have a moveable stage (Sec. 3.1.4). The original dosage and physical mask (Sec. 5.2) experiments were done with the wafers spring mounted between a grounded aluminum piece and a stainless steel aperture to which was spot-welded a Copper mesh with a periodicity of 2000 lines per inch (Fig.4.1). This piece was mounted in the vacuum system using Kimball Physics Groove Grabbers.

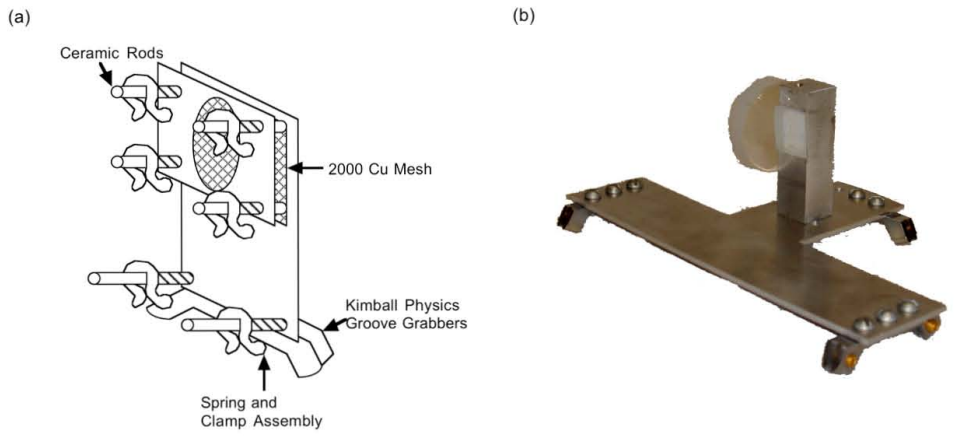

Figure 4.1: (a) Diagram of the first sample mount for the mesh masked experiments. The sample was clamped between two plates and a mesh.
(b) Photograph of the first sample mount for the light mask experiments. The wafer was mounted on the right angle prism with double sided Scotch tape.

Light mask experiments (Sec. 5.3) were also carried out without the moveable stage. In these experiments the sample was mounted on a right angle prism with Scotch tape. The prism was glued with Torr Seal to a mirror from CVI with a high reflectance coating for 1083 nm. The prism was then mounted on a clamp in the vacuum system and the light mask was aligned to be retro-reflecting from outside the vacuum system (Fig.4.1). This mount had to be partially assembled inside the vacuum system and more often resulted in sample damage.

The exposures performed with both of these sample mounts were timed on a stop watch and shuttered with the manual gate valve that also formed the air-lock.

With the acquisition and programming of the movable stage, the sample mounts were adjusted so they could be easily transferred in and out of the sys-

tem and attached to the stage. The sample mounts are attached to standard 2" by 2" Aluminum pieces machined at Stony Brook that can be interchangeably attached to the stage. For the repetition of the physical mask resolution measurements the sample was spring mounted between two standard eV parts from Kimball Physics. The front piece has a 1.5" diameter opening into which was spot-welded a Nickel mesh with a periodicity of 1500 lines per inch (the price of Copper had increased). The sample was grounded to the vacuum system through the stage.

The base design of the sample mount for the light mask experiments consists of a Thorlabs mirror mount that had been made vacuum compatible (vacuum compatible grease on the screws, anodization stripped) and mounted on one of the Aluminum stage plates. The mirror mount holds a 1" diameter CVI mirror (high reflectance for 1083 nm) to which has been attached a right angle prism using Torr seal. The method of mounting the sample to this base went through several stages of development (Fig.4.2). Initially, the sample was attached to the right angle prism with Scotch tape and then grounded through a clamp on the front. In a second iteration, a stainless steel ledge into which the wafer was slipped, was attached to the right angle prism. This mount did not successfully hold the sample perpendicular to the mirror. The final iteration of the sample holder consists of two Aluminum pieces that clamp to the right angle prism and hold the wafer between two slits. The wafer is centered with nylon screws and grounded through the clamp to the stage. This mount is straightforward to load and unload, but can only hold samples large enough for one or two exposures. The exposures are controlled and timed with the stage control program (Sec. 3.1.4) that also measures the atomic beam.

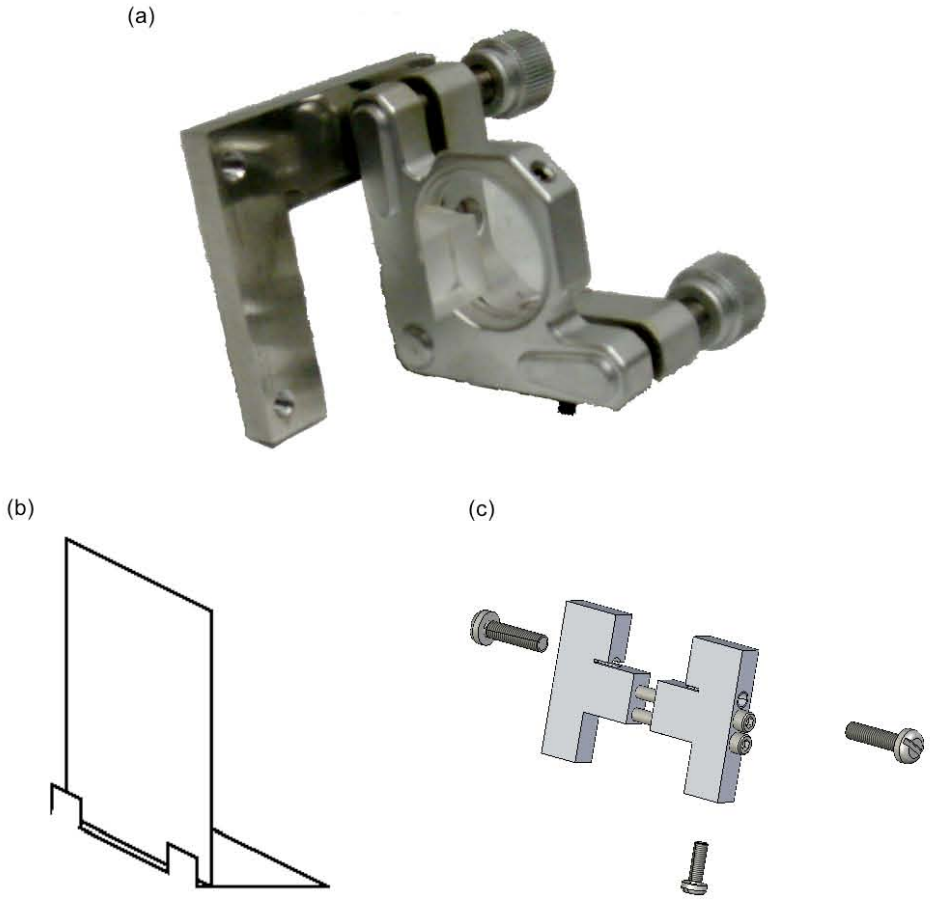

Figure 4.2: (a) Photograph of the mirror mount. For the first light mask experiments in the new system the wafer was mounted on the right angle prism with double sided Scotch tape.
(b) Diagram of steel ledge used to hold the sample. The sample was slipped between the tabs, then the ledge was attached to the right angle prism with vacuum grease.
(c) Diagram of the wafer clamp mount (courtesy of Stony Brook machine shop). The mount clamps around the right angle prism and the wafer slips into the slits and is centered with nylon screws.

4.4 Etch Procedure

Once the wafer with the resist has been exposed and patterned by the He^* beam, the patterns are permanently transferred to the Au using a wet chemical etch developed by Xia et. al. [8]. It is a ferri/ferrocyanide based solution with the concentrations given in Table 4.3. The Potassium Thiosulfate is obtained from Riedel-de Haën, the Potassium Ferricyanide and the Potassium Ferrocyanide are from Sigma-Aldrich and the Potassium Hydroxide is from Fisher Scientific.

Name	Chemical Formula	c [mol/l]	Amount
Potassium Hydroxide	KOH	1	15.586 g
Potassium Thiosulfate	$K_2S_2O_3$	0.1	4.758 g
Potassium Ferricyanide (III)	$K_3Fe(CN)_6$	0.01	0.823 g
Potassium Ferrocyanide (II) Trihydrate	$K_4Fe(CN)_6 \cdot 3\,H_2O$	0.001	0.106 g
Distilled Water	H_2O	solvent	250 ml

Table 4.3: Chemicals used for the chemical etching solutions. The amount given in the last column is for 250 ml of etching solution. Potassium hydroxide naturally contains 10-15% water. For the weight calculation a water content of 10% of the weight is assumed.

The weight of the chemicals is determined with a lab scale of accuracy 2 mg. The constituents are dissolved in water directly before use and mixed with a magnetic stirrer until the solution is bright yellow. The wafer is put into the etching solution for $5 - 10$ minutes. During that time the magnetic stirrer is still on at a low speed ($100 - 300$ rpm) to get a more homogeneous etching process. To avoid direct contact of the stirrer with the wafer, a large beaker is used and the stirrer and the wafer are positioned on opposite sides within the beaker.

The etching of the gold happens in a two step electrochemical process consisting of (1) metal oxidation (dissolution)

$$\mathrm{Au}^0 + 2\mathrm{S_2O_3}^{2-} = \mathrm{Au}\left(\mathrm{S_2O_3}\right)_2{}^{3-} + e^- \tag{4.1a}$$

or

$$\begin{aligned} \mathrm{Au}^0 + 2\mathrm{OH}^- &= \mathrm{Au}\left(\mathrm{OH}\right)_2{}^- + e^- \\ \mathrm{Au}\left(\mathrm{OH}\right)_2{}^- + 2\mathrm{S_2O_3}^{2-} &= \mathrm{Au}\left(\mathrm{S_2O_3}\right)_2{}^{3-} + 2\mathrm{OH}^- \end{aligned} \tag{4.1b}$$

and (2) reduction of an oxidizer

$$\mathrm{Fe}\left(\mathrm{CN}\right)_6{}^{3-} + e^- = \mathrm{Fe}\left(\mathrm{CN}\right)_6{}^{4-} \tag{4.2}$$

The etching solution also works without ferrocyanide, but with it the defects formed in the part covered by the SAM are significantly reduced.

After the etch the wafer is rinsed with distilled water and a short Piranha bath to get rid of residues of the etching solution and the SAM. Once the sample is clean, it is analyzed in a Q-Scope 450 atomic force microscope (AFM) from Quesant (now Ambios Technologies) in our laboratory, or a Zeiss/LEO 1550 Schottky Field Emission Gun scanning electron microscope (SEM) housed in the Materials Science department at Stony Brook University.

Chapter 5

Results

The results from this thesis fall into three three sections. First, numerical simulations determined the acceptable atomic beam and laser parameters to accomplish the focussing and channeling of He*. Second, measurements were made in order to determine the lithographic resolution achievable in our laboratory. Finally, the focussing and channeling experiments were accomplished.

5.1 Numerical Simulations

The numerical simulations of atomic trajectories were inspired by work done at NIST [47] exploring the location of the principal plane of the micro lenses resulting from a standing wave of light (Sec. 1.1). This work demonstrated numerically that in order to set the principle plane of the micro lenses at the center of the standing wave, the power, P_0, of the light in each beam of the

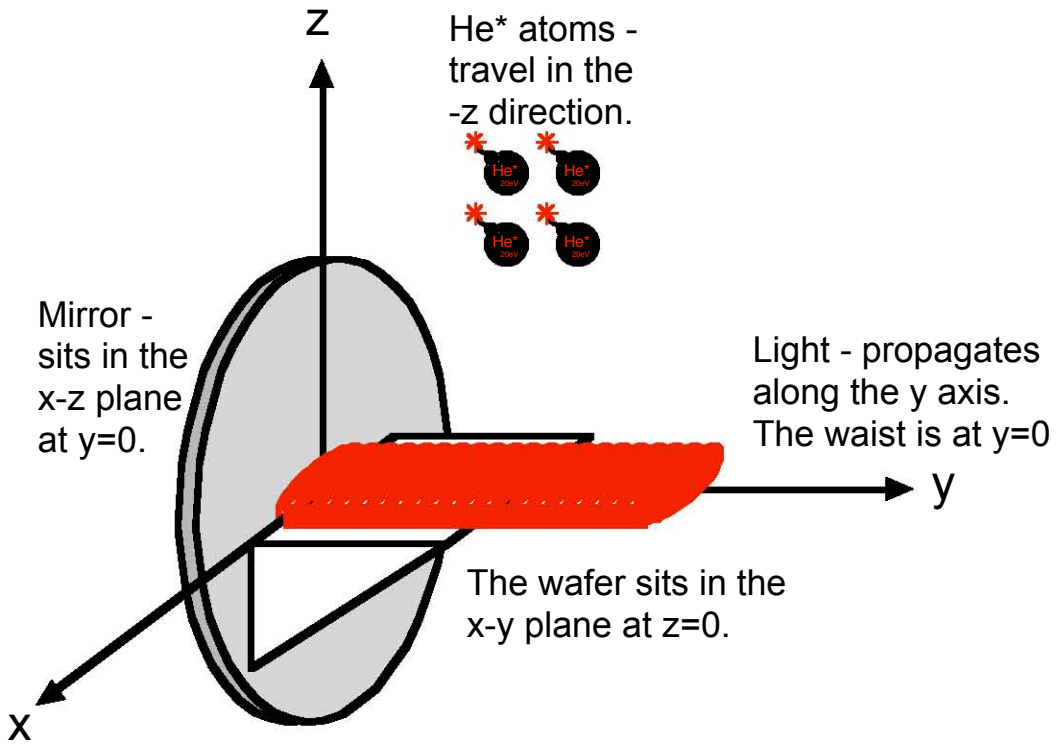

Figure 5.1: Diagram of the coordinate system used for the numerical simulations as it relates to the atomic beam, wafer, mount and light mask.

standing wave satisfied the relation

$$\mathrm{P}_0 = \frac{\pi w_{ox} w_{oz}}{8} 5.37 \frac{m_{\mathrm{He}^*} v_z^2 I_{sat} (\gamma^2 + 4\delta_{LM}^2)}{\hbar \delta_{LM} k^2 w_{oz}^2 \gamma^2} \tag{5.1}$$

given in S.I. units, where δ_{LM} is the detuning of the standing wave from atomic resonance and w_{oz} and w_{ox} are the Gaussian waists of the standing wave with the coordinate system shown in Fig. 5.1. With the principle plane of the lenses set in the center of the standing wave lens array, we defined the focussing regime as when the atoms just reach the axis perpendicular to the principle plane and the channeling regime as where the atoms cross

the axis multiple times while traversing the standing wave (Fig. 5.2). Those calculations determined the initial parameters attempted for the light mask experiment.

5.1.1 Trajectory Calculations

Initial semi-classical numerical simulations were done to confirm that atoms traveling at the average longitudinal velocity of our source with a zero transverse velocity would undergo focussing using the parameters available to our light mask laser (Fig. 5.2). The standing wave light mask detuning of $\delta = 2\pi \times 490$ MHz $\approx 300\gamma$ is the same as that used in the experiment. For the purpose of the calculations this is taken to be far enough from resonance, and the interaction time is short enough that the primary force on the atoms results from the periodic light shift created by the standing wave (Sec. 1.3.3) and all other resonant forces can be ignored. Also, the diffraction effects of the wafer cutting into the light mask are ignored. This was done for expediency and justified with experimental evidence of atomic manipulation with a light mask in other species (Sec. 1.1).

The trajectories of atoms crossing the perfectly retro-reflected laser beam are then calculated by a stepwise integration of the classical equations of motion with the force arising from the quantum mechanical nature of the atom - light interaction. The time steps were 1/1000 of the amount of time required for the atom to reach the center of the standing wave light mask from 5 w_{oz} away - approximately 2 ns.

By changing the power in the light mask beam (P_{LM}) there was a smooth

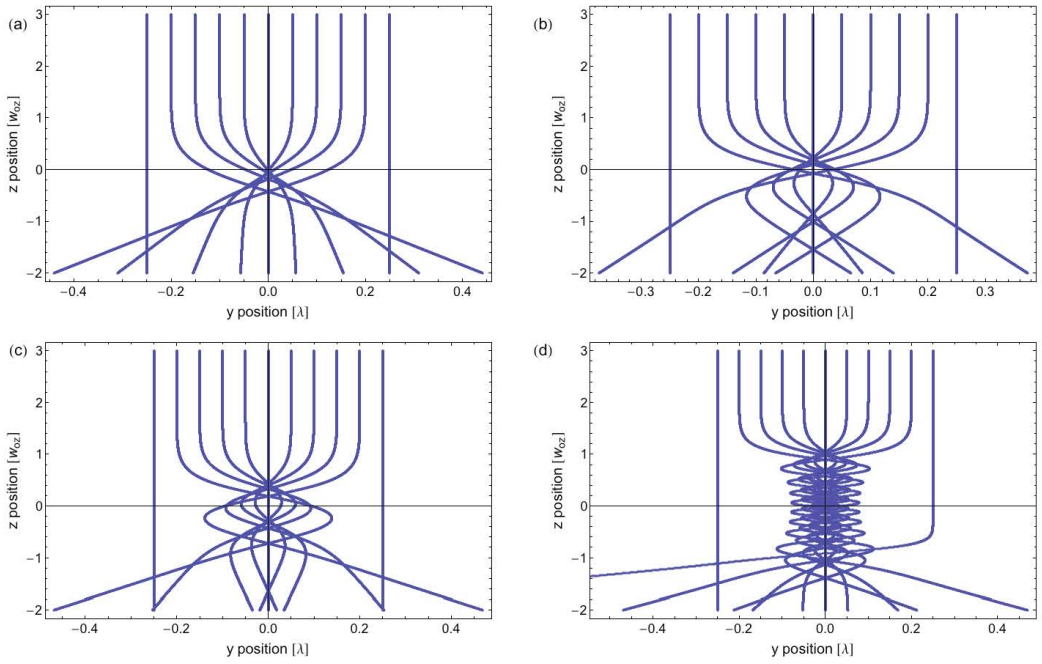

Figure 5.2: With zero longitudinal chromaticity and divergence in the atomic beam, focussing is easily achieved in the center ($w_{oz} = 0$) of the perfect standing wave light mask in agreement with [47]. As the power of the light mask is increased, there is a smooth transition from the focussing to the channeling regime: (a) Each beam has power $\mathrm{P_{LM}} = \mathrm{P_0}$. (b) $\mathrm{P_{LM}} = 2\,\mathrm{P_0}$. (c) $\mathrm{P_{LM}} = 4\,\mathrm{P_0}$. (d) $\mathrm{P_{LM}} = 64\,\mathrm{P_0}$.

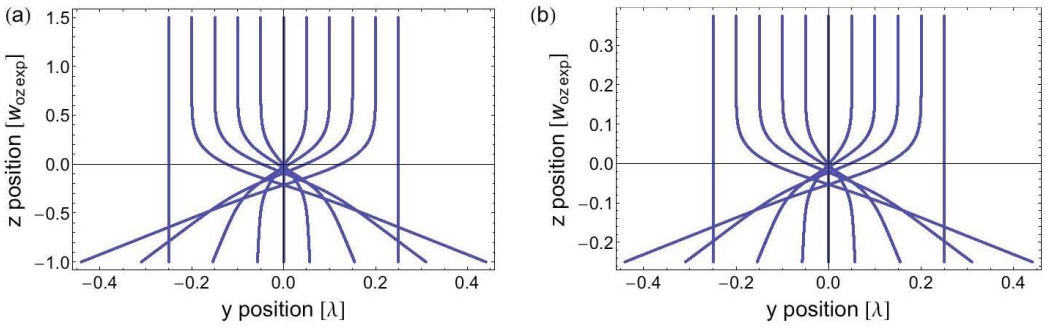

Figure 5.3: As the waist parallel to the atomic beam is changed there is no qualitative difference in the atomic trajectories. (a) $w_{oz} = \frac{1}{2} w_{oz\,\mathrm{exp}}$. (b)$w_{oz} = \frac{1}{4} w_{oz\,\mathrm{exp}}$.

transition from the focussing to the channeling regime (Fig. 5.2). It was also observed that changing the waist of the light mask beam, if it was taken into account in the light mask power calculations derived from [47], did not qualitatively alter the trajectories (Fig. 5.3). These calculations also indicated that the periodic 10% drift in laser power which results from the lab environment increased the width of the focus, but did not wash out the pattern of the lines.

5.1.2 Monte Carlo Simulations

Once the focussing and channeling regimes had been confirmed, a set of Monte Carlo simulations were done to better represent the behavior of the experiment (See Ap. A). These simulations take into account the chromaticity and divergence of the atomic beam. For most of these calculations, the initial atomic population (Fig. 5.4) consists of 2500 atoms $3w_{oz}$ above the center of the light mask with a pseudo random position distribution over an area $4w_{ox} \times \lambda$, where $\lambda = 1083$ nm is the wavelength of the atomic transition. The longitudi-

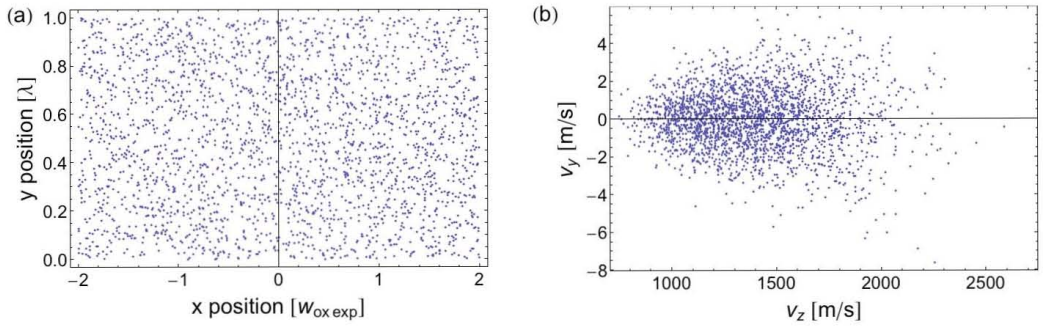

Figure 5.4: An initial atomic distribution containing 2500 atoms. (a) The position distribution is fully pseudo random over the area. (b) The velocity distribution is derived by generating the v_z as a pseudo random value from a Maxwellian distribution and then multiplying it with a pseudo random divergence angle from a Gaussian distribution.

nal velocity of the distribution is pseudo random number from a Maxwellian distribution centered at $v_z = 1125\,\mathrm{m/s}$ and a full width of 440 m/s. The transverse velocity parallel to the direction of propagation of the light mask (v_y) is calculated from a pseudo random divergence angle from a Gaussian distribution with a width of 1.1 mrad. The transverse velocity perpendicular to the direction of propagation of the light mask (v_x) is taken to be zero; because for the purpose of this calculation, the light mask beam is taken to be too large in that dimension to fully expel the atoms and we wished to conserve computing power.

For the calculation of the force on the atoms, the entire population was assumed to be in the $m_J = 1$ sub level and the light mask is composed of σ^+ light so that optical pumping is neglected, and the transition is at its full strength. The numerical integration of the equations of motion is done with time steps of 500 ps as long as the atom is above the wafer surface in the simulation. Given the mean velocity of the atoms, it takes 400 ns for the

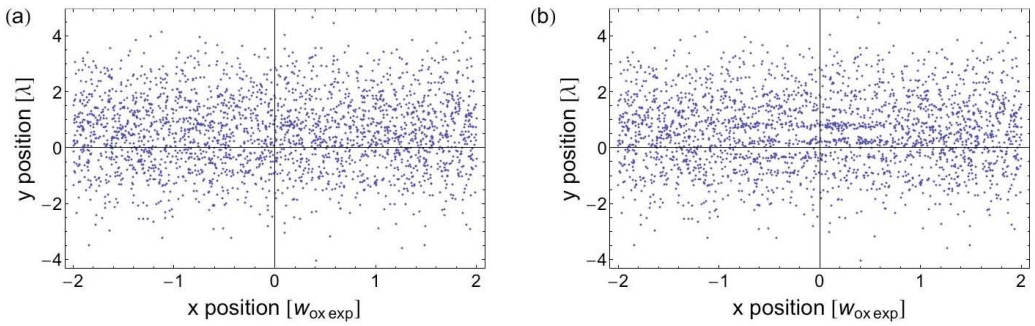

Figure 5.5: Patterning is not observed in the focussing regime of the Monte Carlo calculation, but it is seen in the channeling regime. (a) $P_{LM} = P_0$. (b) $P_{LM} = 4P_0$

atoms to travel w_{oz}. From these Monte Carlo calculations we generated expected exposure maps of various wafer-light mask configurations. The light mask beam was maintained as perfectly retro-reflected and the wafer was kept normal to the retro-reflecting mirror. In order to obtain more accurate periodicity information on the exposure maps generated from these simulations, atomic population size and exposure area were increased. The larger calculations do not generate as nice exposure maps. These maps are binned into areas $0.5w_{ox} \times 0.1\lambda$ and then transformed using a discrete Fourier transform algorithm provided by Mathematica. The resulting transforms give a large DC peak in addition to the spectral components from the patterning.

In the focussing regime ($P_{LM} = P_0$) with the light mask beam waists that are in the experiment, these simulations do not produce an exposure pattern that would result in lines. By tuning the power into the channelling regime, specifically $P_{LM} = 4P_0$, nice parallel lines are observed in the exposure map (Fig. 5.5). In order to determine the primary reason for this, we varied our experimental input parameters while maintaining the focussing condition.

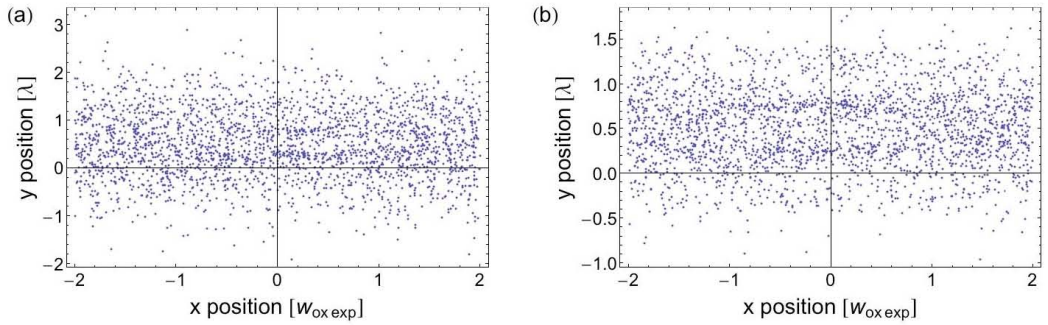

Figure 5.6: The power of the light mask is P_0. Faint lines start to become apparent in the exposure maps as the divergence of the atomic beam is reduced. (a) Atomic beam divergence is taken to be 0.55 mrad. (b) Atomic beam divergence is taken to be 0.275 mrad.

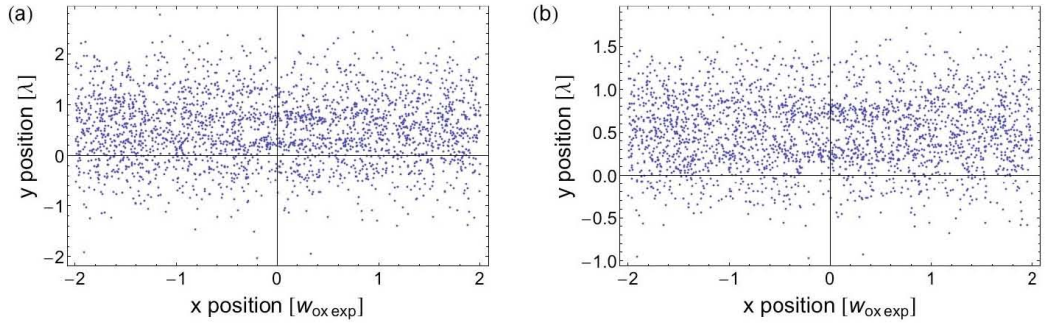

Figure 5.7: The power of the light mask is P_0. Lines start to become apparent in the exposure maps as w_{oz} is reduced. (a) $w_{oz} = \frac{1}{2} w_{oz\,\mathrm{exp}}$. (b) $w_{oz} = \frac{1}{4} w_{oz\,\mathrm{exp}}$.

When the transverse velocity spread is decreased, lines appear in the exposure map (Fig. 5.6). Lines also appear in the focussing regime when the simulation is run with a reduced w_{oz} (Fig. 5.7). Thus, the divergence of the atomic beam seems to be the primary impediment to patterning in the focussing regime.

We also looked at the patterning in the channeling regime at different distances away from the Gaussian waist positioned at the retro-reflecting mirror. When done with a small initial atomic population, these simulations show

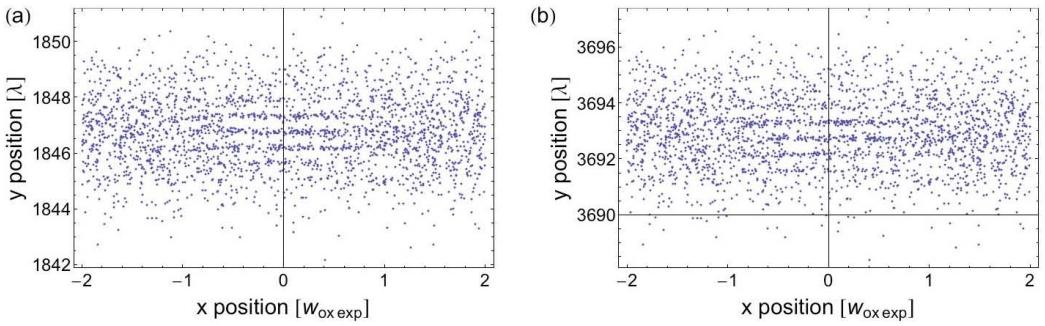

Figure 5.8: Pattering in the channeling regime ($P_{LM} = 4P_0$) at various distances from the retro-reflecting mirror. (a) 2 mm from the retro-reflecting mirror. (b) 4 mm from the retro-reflecting mirror.

negligible qualitative differences at distances reflecting the size of our wafer (Sec. 4.1). Comparing the Fourier transforms of the larger sample calculations by subtracting them from each other, we do not see features comparable to the size of the original spectral peaks.

Finally, in order to determine the requirements concerning the perpendicularity of the light mask to the atomic beam, Monte Carlo simulations were carried out where a v_y offset was added to the initial atomic sample by tilting the angle of the incoming atoms. These calculations were done with the larger samples, again in the channeling regime where the initial simulations indicated that patterning would be easily accomplished. Fourier transforms of the final wafer maps indicated that the atoms must approach the light mask with a central angle less than 5 mrad in order to successfully pattern the wafer.

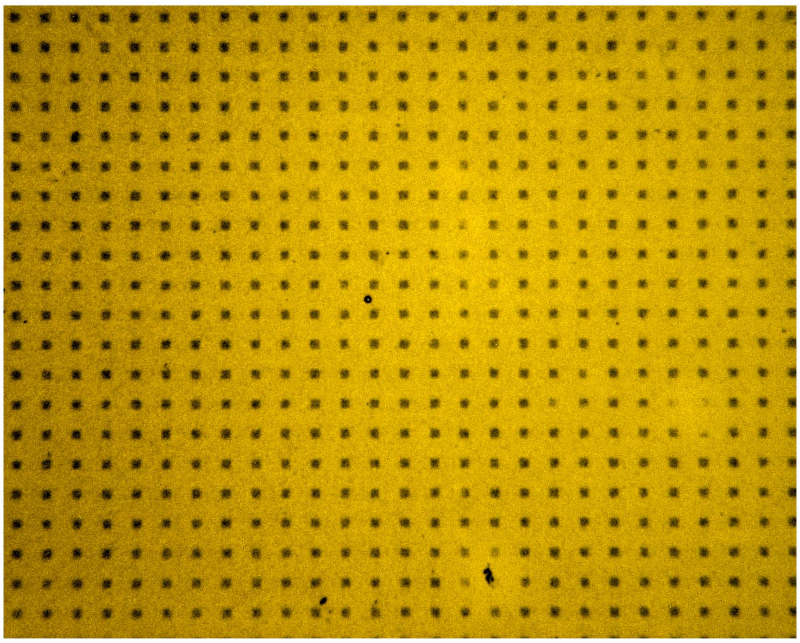

Figure 5.9: Microscope assisted photograph of Au coated Si wafer protected by a micromesh and patterned by He*. Courtesy of Prof. Lukens.

5.2 Experiments With the Mechanical Mask

The first lithography experiments were performed in our lab in 2005 [48] on the predecessor of the current experimental setup. These experiments were performed in order to determine the suitability of our atomic beam for lithography, the effectiveness and reliability of the chemistry, and our ability to image and analyze the resulting structures. These experiments were similar to previous lithography experiments performed with He* [3, 46, 49, 50] and provided similar results. In these experiments the resist covered Au coated Si wafer was patterned by a micromesh during the exposure to the collimated He* beam. The areas of the wafer that were not masked by the wires of the mesh were exposed to the He* beam resulting in damage to the SAM in those areas

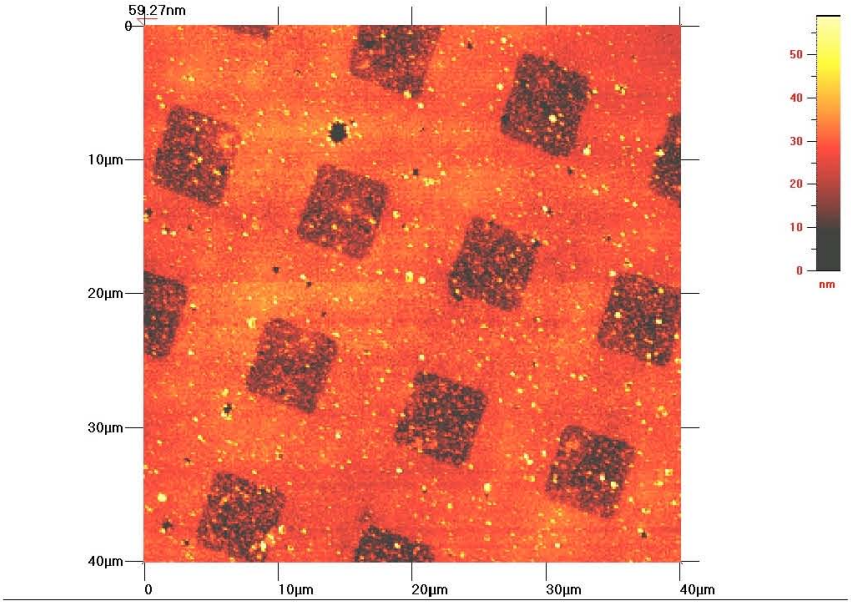

Figure 5.10: A wafer that is under-etched has Au remaining in the areas unprotected by the micro mesh mask. So does a wafer that is under-exposed. The etch and exposure times are dependent on each other and extremely difficult to uncouple.

and so the etch could transfer the pattern of the mesh into the Au (Fig. 5.9).

The experiments performed in 2005 [48] and 2006 [35] with the experimental upgrade, established a reliable peak exposure dose of 3×10^{12} atoms/mm^2. Depending on the quality of the atomic beam, this can result in an exposure time as short as 20 minutes. Wafers exposed to the atomic beam without the atomic collimation to provide adequate dosage did not show evidence of exposure, thus establishing He* as the primary agent for the destruction of the SAM.

The characterization of the etch from these experiments was disappointing. It was observed that while an un-exposed wafer could resist the etch for over one hour; the appropriate etch time for exposed wafers showed great variability

(5 min to 20 min) that did not correlate with exposure time. The etch is timed with its completion determined to be 35% longer than the amount of time in which the area defined by the beam defining slits (See Sec. 3.1.4) becomes discernible from the unexposed areas of the wafer.

While this exposure dose and etch time appeared to give reliable results, it was impossible to recognize a difference in the wafers that were either under-etched or under-exposed (Fig. 5.10). Both of these cases still have remaining gold in the exposed areas which was identifiable by the island nature of the Au layer as seen by the AFM as compared to the smooth surface of the bare Si. Likewise, the over-exposed, under-etched wafers are difficult to differentiate from those with an acceptable exposure dose and slightly longer etch time. Over-etched wafers exhibit full Au removal in the protected areas along the edges of the Au islands where the SAM has not formed a uniform barrier.

The AFM software exports the scans as bitmap files to Mathematica. Here, a least squares fit to the smooth exposed Si wafer is used to remove any tilting in the scan that results from uneven sample mounting and PZT drift in the scan head. The tilt removal is done in Mathematica because algorithms present in the AFM acquisition software do not perform well when the scan size and the feature size are comparable.

The spatial resolution of this technique is taken to be the width of the edge of a structure from 10% to 90% of its height [3]. This measurement required high resolution small area scans in order to provide enough measurements along the edge to obtain a reliable slope. Typical AFM scan parameters for this measurement were a scan size of $5\,\mu\text{m} \times 5\,\mu\text{m}$ and a resolution of 1000, resulting in a pixel size of 5 nm. With the tilt removed from the scan, 100 nm

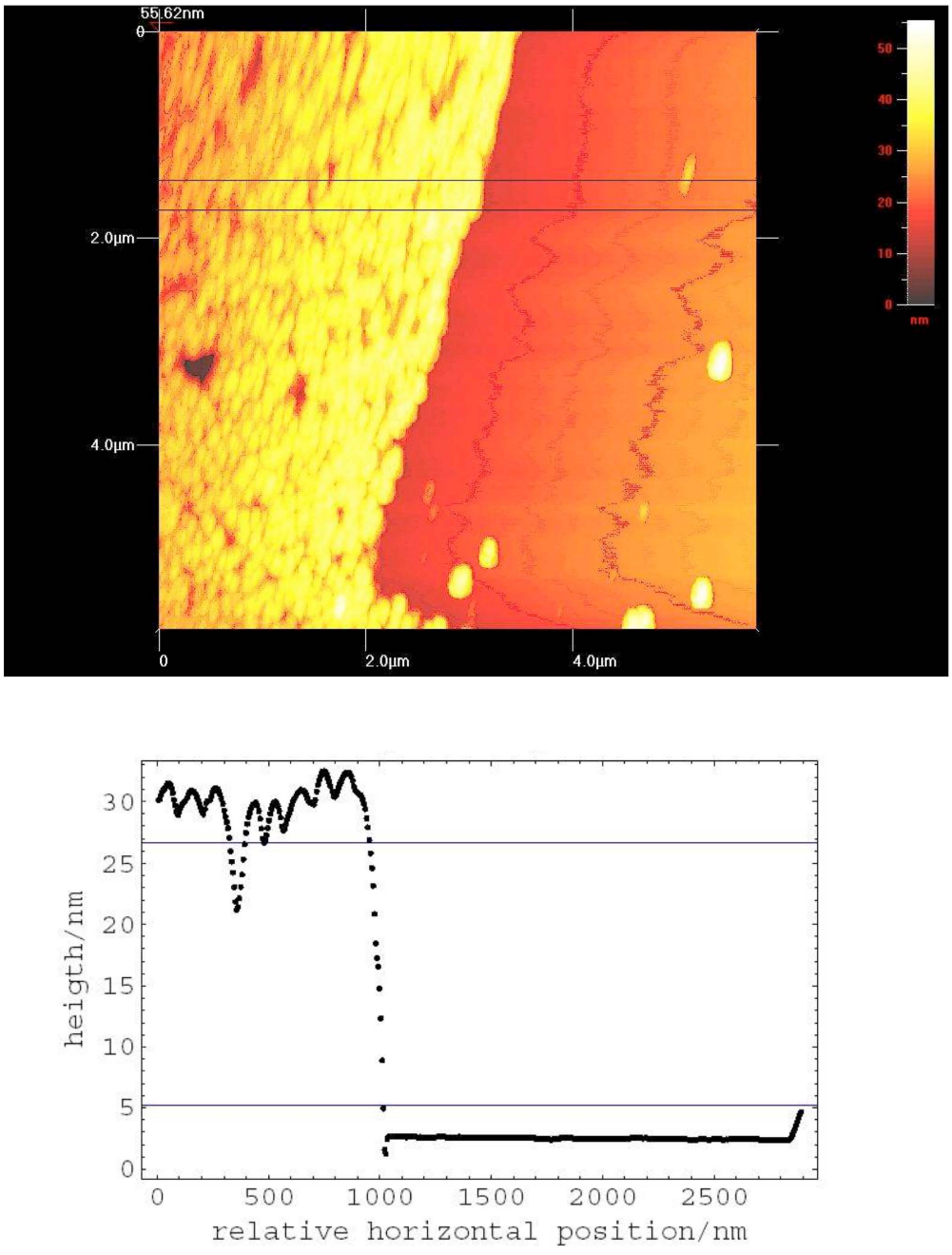

Figure 5.11: The edge resolution is measured as the width of the edge from 10% to 90% of its height. The measurements are taken as an average over an 100 nm wide area. This edge has a resolution of 63 nm. Measured widths span from 13 nm to 100 nm and do not exhibit dependence on exposure parameters.

wide sections perpendicular to the scanned edge are averaged together for the edge width measurement (Fig. 5.11). The typical edge width is approximately 80 nm. We have measured measured widths as small as 13 nm and as large as 100 nm.

5.3 Experiments with the Light Mask

Our first demonstration of patterning an Au coated Si wafer with light mask was with the power of the light mask tuned into the channeling regime. The beams comprising the standing wave light mask had a power $P_{LM} = 4P_0$. The light mask beam was exactly retro-reflected over the sample to within less than 1 mrad, and it was parallel to the last stage Doppler molasses to within 0.3 mrad. These parameters were chosen because the numerical simulations indicated that, with the atomic beam parameters, patterning would be observed on the wafers. The wafers were examined with an AFM and an SEM (Figs. 5.12, 5.13). Lines were also observed by diffraction of white light off the sample (Fig. 5.14).

The AFM scans show a line spacing of 499 $\pm$ 3 nm, which is 10% different from the expected spacing of 542 nm. We believe this arises from inaccuracies in the calibration of the AFM. This conjecture is confirmed from the SEM analysis that shows a spacing of 566 $\pm$ 14 nm. The large error bar seems to arise from a drift in the microscope's calibration at different magnifications and scan resolutions (See Tab. 5.1). Taking a two dimensional fast Fourier transform of the low magnification, high resolution scans we find the spectrum is dominated by a large broad peak that when fit to a Gaussian has a full width

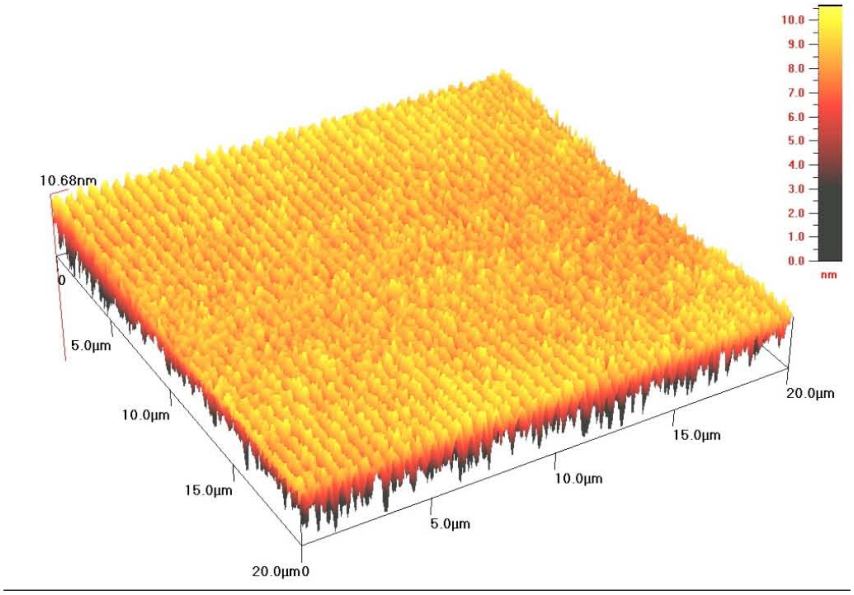

Figure 5.12: AFM scan of patterned wafer with $P = 4P_0$.

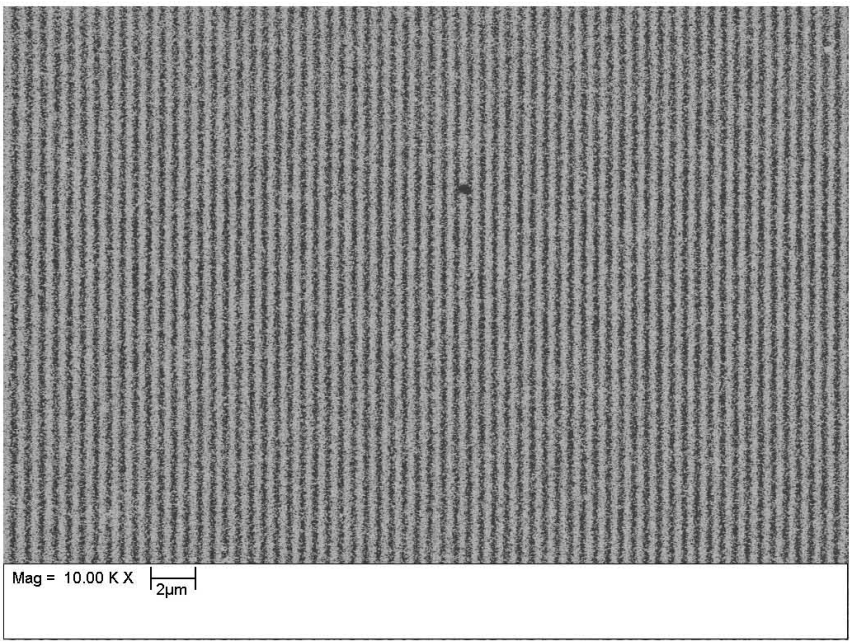

Figure 5.13: SEM Scan of patterned wafer with $P = 4P_0$.

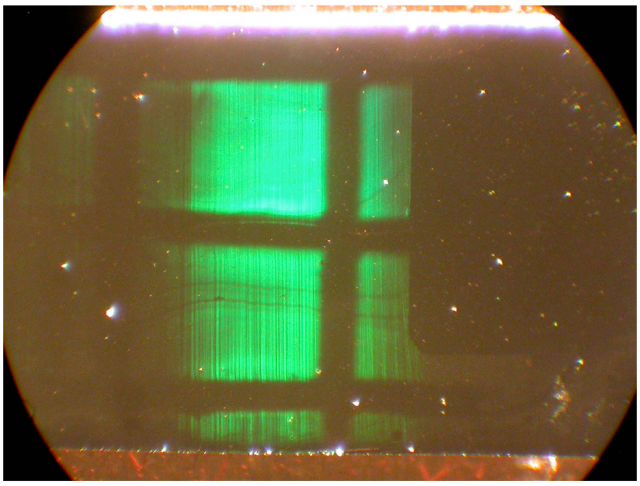

Figure 5.14: Diffraction of white light off the lines of a sample patterned in the channeling regime.

of half the signal length and a signal to noise ratio of 10. The peaks that arise from the periodicity of the lines are twice the height of the broad peak and are transform limited. The width of the lines, approximately 100 nm, has not yet been found to be correlated with exposure dose or etch time. Given that the edge resolution is determined by the quality of the Au coating, SAM and etch time, in a way that we were unable to measure in the experiments described in Sec. 5.2, the expected correlation of the widths of the lines with the light mask power will be difficult to observe.

We have also had difficulty in getting clean patterning where we are certain we have removed all the Au in the lines. While the lines show up clearly on the SEM, we do not get a depth measurement from that microscope. In the measurements on the AFM our most attractive looking patterns will often have depths of no more than 10 nm, which is less than the specified thickness (20 nm) of the Au layer. This indicates that either we are not etching long

Field of View [μm]	Resolution [points]	Line Spacing [nm]	Standard Deviation [nm]
3.81	1042	544	–
12.7	1024	575	8
25.4	1024	549	5
38.1	1024	574	8
38.1	3072	552	–
76.2	3072	546	0
127	1024	563	13

Table 5.1: There is a drift in the SEM calibration as the magnification and scan resolution are changed. THus the spacing measurements from the SEM change with the scan resolution and field of view.

enough to remove the Au from within the lines; or in the area outside of the lines the SAM is damaged enough that some of that area is becoming susceptible to the etch at a slower rate. The AFM does indicate a structure within the exposed area somewhat similar to that which could be expected of a circular beam with a higher intensity in the center: the patterns towards the center of the exposed areas tend to be deeper than those at the edges, which eventually fade to patterns that can only be observed through the Fourier transforms of the scans.

Surprisingly, patterning in the focussing regime was also observed (Fig. 5.15). These samples were primarily analyzed under the SEM which seems to be the more sensitive measure of pattern presence. When these samples were analyzed under the AFM, the patterning was difficult to pick out with the naked eye, but it was evident in the Fourier transforms of those scans. We believe that we may have been able to observe focussing that was not predicted by the numerical simulations because of an over-estimation of the transverse velocity spread.

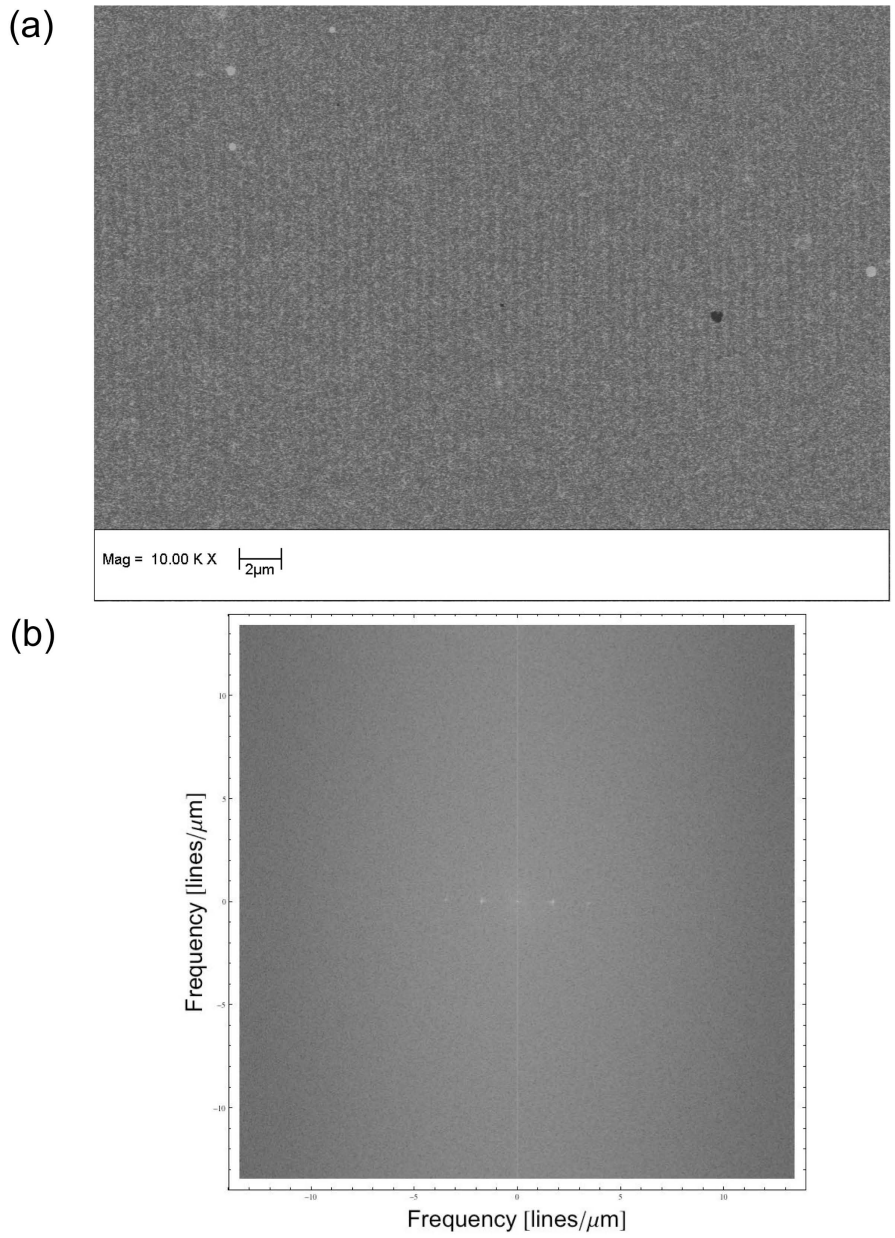

Figure 5.15: (a) SEM Scan of Wafer Patterned with the Light Mask with $P_{LM} = P_0$. The numerical simulations indicated that we should not have seen patterning in this regime given our atomic beam and light mask parameters. The patterning is very faint. (b) A two dimensional Fourier transform of the SEM scan. The peaks indicate the lines in the SEM scan are spaced approximately 500 μm apart.

In the numerical simulations we randomly matched a pseudo-random divergence angle with a pseudo-random longitudinal velocity in order to produce a transverse velocity spread. It is likely that when taking a cross section of the atomic beam, there is a non-uniform distribution of longitudinal and transverse velocities. This could result because atoms with a lower initial longitudinal velocity (v_z) spend more time in the collimation regions, thus attaining a lower transverse velocity and probably mostly populating the center of the atomic beam.

In addition, atoms with a lower v_z that are for some reason not transversely cooled as well, for example those starting in sublevels $m_J = 0$ or 1, will end up on the outside of the atomic beam. Also, the atoms with a higher initial longitudinal velocity will not be as well collimated. Given the complexity of this convolution, it was not attempted in the numerical simulations, but experimentally it seems that there are parts of the atomic beam with slow enough atoms for focussing to work with these light mask beam parameters.

In order to determine the robustness of the channeling experiment, the light mask beam was tilted with respect to the last Doppler molasses beam. This effectively gives the atoms a non-zero central transverse velocity with respect to the direction of propagation of the light mask beam. In previous similar work it was implied that in order for successful patterning even further into the channeling regime, the light mask and the atomic beam had to be exactly perpendicular [18, 51]. In addition, the numerical simulations indicated patterning required an angle less than 5 mrad. The experiments were performed in the channelling regime ($P_{LM} = 4P_0$) with the light mask beam up to 30 mrad away from normalcy with the atomic beam. Patterning was observed

on all the wafers with no observable qualitative difference as compared to the previously described wafers. We believe this to be a result of the mismatch between the simulation and experimental situations as described above.

Chapter 6

Conclusions and Future Work

6.1 Conclusions

We have successfully demonstrated initial numerical modeling of pattern generation through a light mask and methods of pattern generation using resist assisted lithography with He*.

The numerical modeling of the pattern generation established approximate parameters required for experimental success. The greatest source of disagreement between the modeling and experiment arose from an inaccurate model of the transverse velocity distribution of the atomic beam. Given the complex nature of the convolution necessary to produce an accurate distribution, this problem was not pursued and the model is taken as an upper limit of the experimental parameters.

With a mechanical mask we were able to establish exposure parameters and measure the edge resolution of the structures. In varying the exposure parameters we did not see a correlation with the edge resolution. This indicates

that the edge resolution is primarily limited by the wafer and the chemistry, which is in agreement with previous lithography studies (Sec. 1.1).

In light mask experiments we demonstrated one dimensional patterning through a standing wave in both the channeling and focussing regimes. We found unsurprisingly, that the patterns generated with the light mask set to the channeling regime were sharper than those generated with the light mask set to the focussing regime. In addition, we demonstrated that the previously assumed stringent requirement on the alignment of the light mask to the atomic beam is not necessarily valid.

6.2 Future Work

With some modifications to the setup, the light mask patterning of He* can be extended into two dimensions. Initial unsuccessful attempts have been made at generating a two dimensional pattern by skewing the retro-reflection of the light mask beam in the plane of the sample. It is likely this results either from a misunderstanding of the light mask created by the skewed beams or from the larger divergence of the atomic beam in the dimension perpendicular to the current one dimensional patterning. Modifications to the atomic beam system will allow further collimation in the second dimension. Also, methods using multiple mirrors and polarizations will generate light fields with more defined two dimensional structuring. Holograms can also be used to modify the light mask creating more complex higher order patterns eventually resulting in an exploration of the ability to tailor a light field that will serve as a mask to generate an arbitrary complex lithographic pattern.

While this work has successfully produced repeatable patterning, it is possible that either a different substrate or substrate handling procedure may improve the quality of the results. A better measurement of the width of the patterned lines could be obtained with a smoother Au coating. Annealing the Au layer before depositing the SAM can result in larger domains in the Au coating and thus a more uniform resist. Replacing the underlying Si wafer with Muscovite mica or the Au with Palladium can also result in a smoother coating. It has also been suggested that more uniform SAM's are created when the thiols are dissolved in a Triton X-100 and water mixture instead of ethanol for assembly on the Au surface [52]. Another group has suggested increased reproducibility with post exposure treatment of the SAM by adding a polymer to the undamaged SAM or replacing the damaged SAM's with carboxylic terminated alkanethilols [45].

With another He* transition accessible at 389 nm, an improvement in the substrate resolution will facilitate patterning at this wavelength. These structures would have a periodicity smaller than the wavelengths of light in the entire visible spectrum which has exciting implications for the fabrication of left handed materials [53].

Bibliography

[1] M. Prentiss, G. Timp, N.Bigelow, R.E. Behringer, and J.E.Cunningham. Using light as a stencil. *Appl. Phys. Lett.*, 60(8):1027–1029, 1992.

[2] K.K. Berggren, A. Bard, J.L. Wilbur, J.D.Gillaspy, A. Helg, J.J. McClelland, S.L.Rolston, W.D. Phillips, M.Prentiss, and G.M. Whitesides. Microlithography by using neutral metastable atoms and self-assembled monolayers. *Science*, 269(5228):1255–1257, 1995.

[3] S. Nowak, T. Pfau, and J. Mlynek. Nanolithography with metastable helium. *Appl. Phys. B.*, 63:203–205, 1996.

[4] S. Rehse, A. Glueck, S.A. Lee, A.B. Goulakov, C.S. Menoni, D.C. Ralph, K.S. Johnson, and M. Prentiss. Nanolithography with metastable neon atoms: Enhanced rate of contamination resist formation for nanostructure fabrication. *Appl. Phys. Lett.*, 71(10):1427–1429, 1997.

[5] M. Kueis, F. Lison, D. Haubrich, D. Meschede, S. Nowak, T. Pfau, and J. Mlynek. Pattern generation with cesium atomic beams at nanometer scales. *Appl. Phys. B.*, 63:649–652, 1996.

[6] E. Arimondo. Laser controlled nanodeposition of neutral atoms. *Appl. Surf. Sci.*, 248:167–171, 2005.

[7] A. Camposeo, O. Marago, B. Fazio, B Klöter, D. Meschede, U. Rasbach, C. Weber, and E. Arimondo. Resist-assisted atom lithography with group iii elements. *Appl. Phys. B.*, 85:487–491, 2006.

[8] Y. Xia, Z.M. Zhao, E. Kim, and G. Whitesides. A selective etching solution for use with patterned self-assembled monolayers of alkanetiolates on gold. *Chem. Mater.*, 7:2332–2337, 1995.

[9] K.S. Johnson, K.K. Berggren, A. Black, C.T. Black, A.P. Chu, N.H. Dekker, D.C. Ralph, J.H. Thywissen, R. Younkin, M. Tinkham, M. Prentiss, and G.M. Whitesides. Using neutral metastable argon atoms and

contamination lithography to form nanstructure in silicon, silicon dioxide and gold. *Appl. Phys. Lett.*, 69(18):2773–2775, 1996.

[10] SB. Hill, C.A. Haich, F. B. Dunning, G.K. Walters, J.J. McClelland, R.J. Celotta, H.G. Craighead, J. Han, and D.M. Tannenbaum. Patterning of octadecylsiloxane self-assembled monolayers on Si(100) using Ar($^3P_{0,2}$) atoms. *J. Vac. Sci. Technol. B*, 17(3):1087–1089, 1999.

[11] W. Lu, K. Baldwin, M. Hoogerland, S. Buckman, T.J. Senden, T.E. Sheridan, and R.W. Boswell. Sharp edged silicon structures generated using atom lithography with metastable helium atoms. *J. Vac. Sci. Technol. B*, 16(6):3846–3849, 1998.

[12] J. Zhang, M. Kurahashi, T. Suzuki, X. Sun, and Y. Yamuchi. Microfabrication of silicon using self-assembled monolayer resist and metastable helium beam. *Jpn. J. Appl. Phys.*, 45(10A):8020–8023, 2006.

[13] G. Timp, R.E. Behringer, D.M. Tennant, J.E. Cunningham, M. Prentiss, and K.K. Berggren. Using light as a lens for submicron, neutral-atom lithography. *Phys. Rev. Lett.*, 69(11):1636–1639, 1992.

[14] J. J. McClelland, R.E. Scholten, E.C. Palm, and R.J. Celotta. Laser-focused atomic deposition. *Science*, 268(5135):877–880, 1993.

[15] Th. Schulze, B. Brezger, R. Mertens, M. Pink, T. Pfau, and J. Mlynek. Writing a superlattice with light forces. *Appl. Phys. B.*, 70:671–674, 2000.

[16] A. Camposeo, F. Cervelli, F. Tantussi, M. Lindholdt, F. Fuso, M. Allegrini, and E. Arimondo. Atomic nanofabrication by laser manipulation of a neutral cesium beam. *Mat. Sci. Eng. C*, 23:1087–1091, 2003.

[17] K.H. Johnson, J.H. Thywissen, N.H. Dekker, K.K Berggren, A.P. Chu, R.Younkin, and M.Prentiss. Localization of metastable atom beams with optical standing waves: nanolithography at the Heisenberg limit. *Science*, 280(5369):1583–1586, 1998.

[18] P.Engels, S. Salewski, H. Levsen, K. Sengstock, and W. Ertmer. Atom lithography with a cold, metastable neon beam. *Appl. Phys. B.*, 69:407–412, 1999.

[19] J.H. Thywissen, K.H. Johnson, N.H. Dekker, A.P. Chu, and M. Prentiss. Using neutral atoms and standing light waves to form a calibration artifact for length metrology. *J. Vac. Sci. Technol. B*, 16(6):3841–3845, 1998.

[20] J.J. McClelland, W.R. Anderson, C.C. Bradley, M. Walkiewicz, R.J. Celotta, E. Jurdik, and R.D. Delattes. Accuracy of nanoscale pitch standards fabricated by laser-focused atomic deposition. *J. Res. Natl. Inst. Stand. Technol.*, 108:99–113, 2003.

[21] J. Thywissen and M. Prentiss. Demonstration of frequency encoding in neutral atom lithography. *N. J. Phys.*, 7:47, 2005.

[22] R. Gupta, J.J. McClelland, P.Marte, and R.J. Celotta. Raman-induced avoided crossings in adiabatic optical potentials: observation of a $\lambda/8$ spatial frequency in the distribution of atoms. *Phys. Rev. Lett.*, 76(25): 4689–4692, 1996.

[23] Th. Schulze, B. Brezger, P.O. Schmidt, R. Mertens, A.S. Bell, T. Pfau, and J. Mlynek. Sub-100nm structures by neutral atom lithography. *Micro. Elec. Eng.*, 46:105–108, 1999.

[24] R. Shankar. *Principles of Quantum Mechanics*. Plenum Press, New York, 2nd edition, 1994.

[25] D.J. Griffiths. *Introduction to Quantum Mechanics*. Prentice Hall, New Jersey, 1994.

[26] D. Wineland and W. Itanco. Laser cooling of atoms. *Phys. Rev. A*, 20: 1521–1540, 1979.

[27] V.G. Minogin and O.T. Serimaa. Resonant light pressure forces in a strong standing laser wave. *Opt. Comm.*, 30(3):373–379, 1979.

[28] H.J. Metcalf and P. van der Straten. *Laser Cooling and Trapping*. Graduate Texts in Contemporary Physics. Springer, Berlin, 2002.

[29] M.T. Cashen. *Optical Forces on Atoms in Polychromatic Light Fields*. PhD thesis, SUNY Stony Brook, Stony Brook, NY, May 2002.

[30] X. Miao. *Optical Force on Atoms with Periodic Adiabatic Rapid Passage Sequences*. PhD thesis, SUNY Stony Brook, Stony Brook, NY, August 2006.

[31] X. Miao, E. Wertz, M. G. Cohen, and H. Metcalf. Strong optical forces from adiabatic rapid passage. *Phys. Rev. A*, 75(1):011402, Jan. 2007.

[32] J. S. Hack. *Laser Cooling in the Recoil Domain*. PhD thesis, SUNY Stony Brook, Stony Brook, NY, December 2001.

[33] O.A. Kritsun. *Atom Optics with Rydberg States in Inhomogeneous Electric Fields*. PhD thesis, SUNY Stony Brook, Stony Brook, NY, August 2003.

[34] S.H. Lee. *Cotherent Manipulation of Rydberg Helium Atoms in Inhomogenous Electric Fields*. PhD thesis, SUNY Stony Brook, Stony Brook, NY, August 2006.

[35] M.C. Keller. Optical manipulation of helium atoms with application to neutral atom lithography. Master's thesis, SUNY Stony Brook, Stony Brook, NY, August 2006.

[36] M Partlow, X Miao, J Bochmann, M Cashen, and H Metcalf. Bichromatic slowing and collimation to make an intense helium beam. *Phys. Rev. Lett.*, 93(21):213004, Nov 2004.

[37] J. Bochmann. Atomic beam collimation using the bichromatic force. Master's thesis, SUNY Stony Brook, Stony Brook, NY, August 2004.

[38] M.J. Partlow. *Bichromatic Collimation to Make an Intense Helium Beam*. PhD thesis, SUNY Stony Brook, Stony Brook, NY, December 2004.

[39] I.S. Shahin T.W. Hänsch and A.L. Schawlow. High-resolution saturation spectroscopy of the sodium d lines with a pulsed tunable dye laser. *Phys. Rev. Lett.*, 27(11):707–710, Sept. 1971.

[40] J. Kawanaka, M. Hagiuda, K. Shimizu, F. Shimizu, and H. Takuma. Generation of an intense low-velocity metastable-neon atomic beam. *Appl. Phys. B: Lasers Opt.*, 56:21–24, 1993.

[41] HC Mastwijk, JW Thomsen, P van der Straten, and A Niehaus. Optical collisions of cold, metastable helium atoms. *Phys. Rev. Lett.*, 80(25): 5516–5519, June 1998. ISSN 0031-9007.

[42] F. B. Dunning, R. D. Rundel, and R. F. Stebbings. Determination of secondary electron ejection coefficients for rare gas metastable atoms. *Rev. Sci. Instrum.*, 46(6):697–701, 1975.

[43] H. Klein, W. Blanc, R. Pierrisnard, C.Fauquet, and Ph. Dumas. Self-assembled monolayers of decanetiol on Au(111)/mica. *Eur. Phys. J. B*, 14(2):1434–6028, 2000.

[44] F. Schreiber. Sturcture and growth of self-assembling monolayers. *Prog. Surf. Sci.*, 65:151–256, 2000.

[45] Michael L. Chabinyc, J. Christopher Love, Joseph H. Thywissen, Federico Cervelli, Mara G. Prentiss, and George M. Whitesides. Self-assembled monolayers exposed to metastable Argon beams undergo Thiol exchange reactions. *La.*, 19:2201–2205, August 2003.

[46] A. Bard, K.K. Berggren, J.L. Wilbur, J.D. Gillaspy, S.L Rolston, J.J. McClelland, W.D.Phillips, M. Prentiss, and G.M. Whitesides. Self-assembed monolayers exposed by metastable argon and metastable helium for neutral atom lithography and atomic beam imaging. *J. Vac. Sci. Technol. B*, 15(5):1805–1810, 1997.

[47] J.J. McClelland. Atom-optical properties of a standing-wave light field. *J. Opt. Soc. Am. B.*, 12(10):1761–1768, October 1995.

[48] M.P. Riedmann. Neutral atom lithography using a beam of metastable helium collimated by bichromatic light. Master's thesis, SUNY Stony Brook, Stony Brook, NY, August 2005.

[49] B. Brezger, Th. Schulze, U. Drodofsky, J. Stuhler, S. Nowak, T. Pfau, and J. Mlynek. Nanolithography with neutral chromium and helium atoms. *J. Vac. Sci. Technol. B*, 15(6):2905–2911, 1997.

[50] A.S. Bell, T. Pfau, U. Drodofsky, T. Stuhler, Th. Schulze, B. Brezger, S. Nowak, and J. Mlynek. Atomic lithography. *Micro. Elec. Eng.*, 41: 587–590, 1998.

[51] S. Petra, L. Feenstra, W. Hogervorst, and W. Vassen. Nanolithography with metastable helium atoms in a high-power standing-wave light field. *Appl. Phys. B.*, 78:133–136, 2004.

[52] V. Ganesh and V. Lakshminarayanan. Self-assembled monolayers of Alkanethiols on Gold prepared in a hexagonal lyotropic liquid crystalline phase of Triton x-100/water system. *La.*, 22(4):1561–1570, Jan. 2006.

[53] S. Anantha Ramakrishna. Physics of negative refractive index materials. *Rep. Prog. Phys*, 68:449–521, Jan. 2005.

Appendix A

Numerical Simulation

The Monte Carlo simulation is written in Mathematica. It is discussed in Section 5.1.2. The code, as written in Mathematica is on the following pages.

Trajectories through a retro-reflected gaussian beam:

This script calculates the trajectories through a directly reflected gaussian beam.

In order to avoid large numbers of imaginary factors with 0 amplitude, the vector $\vec{r}$ is not defined until after the standing wave is fully defined.

Initialization

■ Constants

■ Physical Constants to do with Helium

Sets various constants as given by *Mathematica*. We have to remove the units that they provide

```
<< "PhysicalConstants`"
ħ = PlanckConstantReduced / (Joule Second);
m = ElementData["Helium", "AtomicWeight"] / (AvogadroConstant Mole) 10^-3;(*in kg*)
```

■ Helium Red Transition: $2^3S_1 \rightarrow 2^3P_2$

```
λ = 1.0833 10^-6;(*wavelength in m*)
k = 2 π / λ;(*wave vector magnitude in m^-1*)
γ = 2 π 1.62 10^6; (*decay rate in angular frequency units*)
is = 0.17 10^-3 / (10^-2 10^-2);(*Saturation intensity in W/m^2*)
```

■ Calculation Variables: define space vector and reals

```
{x, y, z, r, t, θ, ϕ, φ} ∈Reals;
```

■ Experimental Parameters

```
vl = 1125;(*velocity out of the source in m/s for fully collimated beam*)
δvl = 440;(*longitudinal velocity spread in m/s for fully collimated beam*)
θt = 1.1 10^-3;(*horozontal atomic beam divergence for full collimation - half angle*)
δlm = 2 π 490 10^6;(*light mask beam detuning, Hz*)
wox = (0.72051 + 0.70636) 10^-3; (*waist perpendicular to the He* beam*)
woz = (0.20836 + 0.20805) 10^-3;(*waist parallel to the He* beam*)
```

■ Gaussian Beam Parameters

The gaussian beam is propagating in the y direction

$$zoz = \frac{\pi\, woz^2}{\lambda};$$

$$zox = \frac{\pi\, wox^2}{\lambda};$$

$$wx = wox\sqrt{1 + \frac{y^2}{zox^2}};$$

$$wz = woz\sqrt{1 + \frac{y^2}{zoz^2}};$$

E-Field from the Light Beam

■ Gaussian Beam Formations for $w_{ox} \neq w_{oz}$.

This follows the derivation of Gaussian Beam formation given in Lasers by Miloni & Eberly Ch14

$$eField = \frac{e^{-i\,\text{ArcTan}[y/zox]/2}}{\sqrt[4]{1 + \left(\frac{y}{zox}\right)^2}}\,\frac{e^{-i\,\text{ArcTan}[y/zoz]/2}}{\sqrt[4]{1 + \left(\frac{y}{zoz}\right)^2}}\, e^{i\,k\,x^2/(2\,y+2\,zox^2/y)}\, e^{i\,k\,z^2/(2\,y+2\,zoz^2/y)}\, e^{-x^2/wx^2}\, e^{-z^2/wz^2}\, e^{i\,(kr-\omega\,t)};$$

$$eFieldC = \frac{e^{i\,\text{ArcTan}[y/zox]/2}}{\sqrt[4]{1 + \left(\frac{y}{zox}\right)^2}}\,\frac{e^{i\,\text{ArcTan}[y/zoz]/2}}{\sqrt[4]{1 + \left(\frac{y}{zoz}\right)^2}}\, e^{-i\,k\,x^2/(2\,y+2\,zox^2/y)}\, e^{-i\,k\,z^2/(2\,y+2\,zoz^2/y)}\, e^{-x^2/wx^2}\, e^{-z^2/wz^2}\, e^{-i\,(kr-\omega\,t)};$$

```
(*This is just the cc, mathematica is funny about taking it*)
```

■ Wave Vectors

This sets up for a plane wave coming in from the +y direction that hits a mirror in the x-z plane. This is for the convenience of drawing the axes

```
k1 = {{0}, {-1}, {0}};(*incoming light*)
k2 = {{0}, {1}, {0}};(*outgoing light*)
```

Write the wave vector in cartesian coordinate form and substitue in the light value

```
kr1 = k Flatten[k1].r;
kr2 = k Flatten[k2].r;

k1 =.;
k2 =.;
```

■ Resulting E fields - SW formulation

Here we write down the e fields of the counter propagating waves

```
eField1 = eField /. kr → kr1;
eField2 = eField /. kr → kr2;
```

We need to write down their complex conjugates separately because mathematica can be funny about taking the cc, and you need to square with the cc's

```
eFieldC1 = eFieldC /. kr → kr1;
eFieldC2 = eFieldC /. kr → kr2;

gausSwave = Chop[ComplexExpand[FullSimplify[(eField1 + eField2) (eFieldC1 + eFieldC2)]][[1]]];
```

If we define the r vector before this point, *Mathematica* had a great deal of difficulty simplifying the equations and ends up carrying around alot of imaginary parts of the field.

```
r = {{x}, {y}, {z}};

gausSwave = Chop[gausSwave];(*Gets rid of numerical zeros*)
```

■ Clean the Kernel

■ E Field Formulation

```
kr1 =.;
kr2 =.;

eField =.;
eFieldC =.;
eField1 =.;
eField2 =.;
eFieldC1 =.;
eFieldC2 =.;
```

■ Gaussian Beam Parameters

The gaussian beam is propagating in the y direction

```
zoz =.;
zox =.;
wx =.;
```

Deriving the Dipole Force

We assume the dipole force in the x and z direction is negligible. Mostly this is because we are concerned about the lines formed in the y direction and the x and z compnents of the motion should not effect this.

■ Time Constant Part

```
deriv = ∂y gausSwave[[1]];
(*derivative of the e-field along the direction of propagaion of the light*)

ipk = 5.37 (m vl^2 is (γ^2 + 4 δlm^2)) / (ħ δlm k^2 wz^2 γ^2) fudge;(*calculated from the McClelland Paper,
fudge is used to change the power by various factors*)
b = (ħ γ^2) / (8 δlm is);(*this is the multiplier that goes in front of the dipole force*)
```

```
force = -b ipk deriv ;(*Time constant light force on the atoms*)

power = (wox woz π)/8 ipk /. y → 0;(*what the power meter needs to read*)
```

■ Time varying part - due to lab conditions

In order to add this into the overal calculation, the atoms have to be sent at the sample in batches separated in time. The fluctuations are slow enough that we assume they do not effect the atoms as they are transversing the beam.

```
hitPeriod = 200;(*number of seconds between atomic populations that hit the sample*)
fluctPeriod = 2000;(*period of lab temp fluctuations in seconds*)

pct = 10;(*Amplitude of fluctuations as a percent of the average power*)

fluct = -(pct/100) b ipk Sin[(2 π)/2000 hitPeriod t] deriv;(*gives the fluctuation amplitude*)
```

Numerical Calculation

■ Target Directory

```
SetDirectory["C:\Documents and Settings\Christopher Allred\My Documents\Claire\Input"];
```

■ File Generator

The atomic distribution is given by an external file. This file has the properties that :
The xy position is fully pseudo random.
The vl distribution is a pseudo random number from a maxwellian distribution.
The vt distribution is calculated by generating a pseudo random divergence angle from a Gaussian distribution and then calculating the resulting vt.

Atomic Sample

```
For[q = 1; initialSample = {}; velocitiesF = {}; velocitiesH = {}; velocitiesQ = {}, q ≤ 5000, q++,

  (*longitudinal velocity: Maxwellian Dist*)
  vlC = Mean[MaxwellDistribution[δvl]] + RandomReal[MaxwellDistribution[δvl]];

  (*Transverse velocity: gaussian distribution of divergence angles*)
  vtCX = vlC * RandomReal[NormalDistribution[0, θtX]]; (*perpendicular to LM propagation*)
  vtCY = vlC * RandomReal[NormalDistribution[0, θtY]]; (*parallel to LM propagation*)

  vtCXH = vlC * RandomReal[NormalDistribution[0, θtX/2]]; (*perpendicular to LM propagation*)

  vtCYH = vlC * RandomReal[NormalDistribution[0, θtY/2]]; (*parallel to LM propagation*)

  vtCXQ = vlC * RandomReal[NormalDistribution[0, θtX/4]]; (*perpendicular to LM propagation*)

  vtCYQ = vlC * RandomReal[NormalDistribution[0, θtY/4]]; (*parallel to LM propagation*)

  (*atomic position*)
  atomsC = {RandomReal[{-2 wox, 2 wox}], RandomReal[{0, λ}]};

  AppendTo[initialSample, atomsC]; (*saves the initial sample x and y information*)
  AppendTo[velocitiesF, {vlC, vtCX, vtCY}];
  AppendTo[velocitiesH, {vlC, vtCXH, vtCYH}];
  AppendTo[velocitiesQ, {vlC, vtCXQ, vtCYQ}];

  atomsC =.;
 ];
```

Export Data Files

Calulation Setup

Timing - this determines the number of steps between the zstart and the wafer

Gives the timing steps

```
n = 2000;(*number of steps between initial and final z positions*)
tStep = zstart/(n vl);
```

Defines the starting and ending position of the atoms in the beam

```
zstart = 3 woz;
zend = 0 (*in units of woz*);
ypos = 0;
```

Gives the factor

```
powerFudge = 4;
```

- **Clean the Kernel**

MonteCarlo

This is a Monte Carlo Simulation. It gives an initial position and velocity distribution and a final position distribution, but discards all other information.
The calculation stop is given by a z position and is controlled by a while loop. Each atom enters the calculation separately.

The entire calculation can easily be put into a loop in order to vary different parameters.

This version does not account for the fluctuations in the foce due to lab conditions.

Define the magnitude and action length of the simulation

```
fudge = powerFudge;
zF = zend * woz;
```

Set up the export file names

```
file1 = ToString[fudge] <> "fudge_" <> ToString[Round[1000 * ypos]] <> "mm_xy.txt";
file2 = ToString[fudge] <> "fudge_" <> ToString[Round[1000 * ypos]] <> "mm_v.txt";
file3 = ToString[fudge] <> "fudge_" <> ToString[Round[1000 * ypos]] <> "mm_z.txt";
file4 = ToString[fudge] <> "fudge_" <> ToString[Round[1000 * ypos]] <> "mm_infoM.txt";
```

Import the initial atomic sample

```
SetDirectory["C:\Documents and Settings\Christopher Allred\My Documents\Claire\Input"];
initAtoms = Import["InitialXY3D.txt", "Table"];
initVs = Import["InitialVF3D.txt", "Table"];
SetDirectory["C:\Documents and Settings\Christopher Allred\My Documents\Claire\Output"];
```

Apply the dipole force to the atomic sample

```
sampleSize = Length[initAtoms];
If[sampleSize ≠ Length[initVs], Abort[]];

(*This loop creates the atomic sample, then applies the force*)
For[j = 1; finalSample = {}; velocities = {}; finalZ = {}, j ≤ sampleSize, j++,

  atomsC = Append[initAtoms[[1]] + {0, ypos}, zstart]; (*atom position*)
  vlC = initVs[[1, 1]]; (*atom velocity*)
  vtC = initVs[[1, 3]]; (*atom velocity*)

  initAtoms = Delete[initAtoms, 1];
  initVs = Delete[initVs, 1];

  (*Apply Force to atoms*)
  While[atomsC[[3]] > zF,
   dvt = force/m tStep /. {z → atomsC[[3]], x → atomsC[[1]], y → atomsC[[2]]};
   vtC = vtC + dvt; (*vtC goes from number to table, this may cause trouble*)
   atomsC =
    {atomsC[[1]](*x position not effected by the force*),
     atomsC[[2]] + vtC * tStep(*y position is changed by the transverse velocity*),
     atomsC[[3]] - vlC * tStep(*zposition is changed by the longitudinal velocity*)};
  ];
  (*End Force Caluclation*)

  AppendTo[finalSample, Drop[atomsC, -1]];
  AppendTo[velocities, {vlC, vtC}];
  AppendTo[finalZ, Take[atomsC, -1]];
  atomsC =.;
  dvt =.;
  vlC =.;
  vtC =.
 ];(*End Atomic Sample Creation*)
```

Records the parameters of the output files

```
info = "theta_t = " <> ToString[θt] <> "\nv_l = " <> ToString[vl] <> "\ndv_l = " <>
   ToString[δvl] <> "\nPower Fudge = " <> ToString[powerFudge] <> "\nPower = " <>
   ToString[power] <> "\nwoz = " <> ToString[woz] <> "\nz_end = " <> ToString[zF] <>
   "\nwafer pos = " <> ToString[ypos] <> "\nz_final = " <> ToString[Mean[finalZ]];
```

Export the data into text files

```
Export[file1, finalSample, "Table"];
Export[file2, velocities, "Table"];
Export[file3, finalZ, "Table"];
Export[file4, info];
```

Exit

```
Remove["Global`*"]
```